**FACULTY
OF MATHEMATICS
AND PHYSICS**
Charles University

BACHELOR THESIS

Tomáš Maleček

Strain influence on magneto-optical properties of La$_{2/3}$Sr$_{1/3}$MnO$_3$

Institute of Physics of Charles University

Supervisor of the bachelor thesis: RNDr. Martin Veis, Ph.D.

Study programme: Physics

Study branch: General Physics

Prague 2020

I declare that I carried out this bachelor thesis independently, and only with the cited sources, literature and other professional sources. It has not been used to obtain another or the same degree.

I understand that my work relates to the rights and obligations under the Act No. 121/2000 Sb., the Copyright Act, as amended, in particular the fact that the Charles University has the right to conclude a license agreement on the use of this work as a school work pursuant to Section 60 subsection 1 of the Copyright Act.

In . . . . date 		. . . .
						Author's signature

i

I would like to thank you, the reader, for taking some time in this hectic world to acquaint yourself with this work.

Title: Strain influence on magneto-optical properties of $La_{2/3}Sr_{1/3}MnO_3$

Author: Tomáš Maleček

Institute: Institute of Physics of Charles University

Supervisor: RNDr. Martin Veis, Ph.D., Institute of Physics of Charles University

Abstract: The influence of epitaxial strain on $La_{2/3}Sr_{1/3}MnO_3$ (LSMO) thin films has been studied by magneto-optical spectroscopy. The investigated samples have been grown by pulsed laser deposition on four different substrates with varying degree of compressive and tensile strain. The spectra of the magneto-optical Kerr effect (MOKE) have been measured. Deterioration of magnetic properties with increasing epitaxial strain has been observed. The off-diagonal elements of the permittivity tensor, numerically calculated from the MOKE and spectroscopic ellipsometry measurements, confirmed two already reported electronic transitions. A third transition at around 4.3 eV has been observed on samples grown under compressive strain. The dependence of the Kerr rotation spectra on temperature has been measured for all four samples. The Curie temperatures have been estimated for all samples with the exception of LSMO grown on $LaAlO_3$ which undergoes a spin reorientation transition at 200 K. The low temperature measurements on the compressively strained samples showed amplification of the third transition supporting the claim of it being paramagnetic. Also observed was a change in the spectra of the Kerr rotation of the sample grown on $SrTiO_3$ which undergoes a structural transition at 105 K, and, therefore, changes the epitaxial strain.

Keywords: magneto-optical Kerr effect, epitaxial strain, Curie temperature

Contents

Introduction

This thesis aims to advance the study of the influence of epitaxial strain on hole doped manganites. Hole doped manganites, given by $La_{1-x}M_xMnO_3$, where M stands for either Ca, Sr or Ba, are thoroughly researched materials [1, 2, 3] due to the unique combination of their physical properties. The most intriguing of which is the combination of colossal magnetoresistance (CMR) [4] and high degree of spin polarization spanning the whole family of hole doped manganites. However, so far no thorough systematic study has been published that would investigate a wide variety of epitaxialy strained samples with respect to temperature.

The particular case of $La_{2/3}Sr_{1/3}MnO_3$ (LSMO) has been subject to extensive research due to it's high Curie temperature ($T_C^{bulk} \approx 370$ K) [5] and almost 100% spin polarization [6]. LSMO is a half-metal, conducting current for only one orientation of the spin and acting as an insulator for the other. Such physical properties make LSMO an auspicious candidate for the application in the field of spintronics.

The ferromagnetic ordering of LSMO has been explained by Zener [7] through a double-exchange (DE) interaction. The DE is an e_g electron transfer between Mn^{3+} and Mn^{4+} ions via the O^{2-} $2p$ state. The probability of this interaction is highly dependent on the Mn^{3+}-O-Mn^{4+} geometry. Thus, the main factors responsible for the change of the magnetic properties of LSMO are the rotations and distortions of the MnO_6 octahedra. Such distortions or rotations are induced in thin films of LSMO by epitaxial strain as a result of the lattice mismatch or by coupling of the octahedral rotations at the sample/substrate interface [8].

The oxygen octahedra coupling (OOC) is restricted to a distance of several monolayers due to it's interfacial nature. The first couple monolayers, which are the most likely to be influenced by OOC, are typically magnetically inert. On the contrary, the thin films of LSMO deposited on mismatched substrates remain fully strained for up to tens of nanometers in thickness, hence proving the importance of the influence of epitaxial strain on the magnetic properties of LSMO.

The majority of theoretical applications of LSMO make use of the effect of strain on the properties of LSMO in a dynamic way. However, for research purposes we have chosen to study the effect of strain on LSMO in a static manner. Depositing LSMO on materials inducing a wide variety of strains ranging from a large compressive strain on $LaAlO_3$ (LAO), through a mild compressive strain on $(LaAlO_3)_{1/3}(Sr_2AlTaO_6)_{2/3}$ (LSAT) and a mild tensile strain on $SrTiO_3$ (STO), up to a large tensile strain on $DyScO_3$ (DSO).

The thesis begins with the origin of the electromagnetic wave. The concept of polarization for such a wave is introduced in the second chapter. This concept is then neatly described using the Jones formalism. Before making use of this formalism in the fourth chapter about experimental methods the thesis introduces the permittivity tensor and the Yeh formalism for the calculation of the magneto-optical response of a sample. After the introduction of the experimental methods the theory of ferromagnetism is presented in chapter five. The last two chapters are then devoted to the introduction of the samples and the measurements and discussion of the results.

1. Electromagnetic waves

Visible light is a small part of the spectrum of electromagnetic waves. In order to study light we have to study the electromagnetic waves. This chapter introduces Maxwell's equations and the electromagnetic constitutive relations. Derived from these equations is the electromagnetic wave equation. A specific solution for the electromagnetic wave equation is presented in the form of a monochromatic time-harmonic plane wave in vacuum.

1.1   Wave equation

The electromagnetic wave equation is derived from Maxwell's equations, constitutive relations and Ohm's law. The most general of these are Maxwell's equations [9] which are universally applicable and link together the electric field $\boldsymbol{E}$, magnetic induction $\boldsymbol{B}$, displacement field $\boldsymbol{D}$, magnetic field $\boldsymbol{H}$, free current density $\boldsymbol{j}_f$ and free charge density ρ_f in the following differential relations

$$\nabla \times \boldsymbol{H} - \frac{\partial \boldsymbol{D}}{\partial t} = \boldsymbol{j}_f \,, \tag{1.1}$$

$$\nabla \cdot \boldsymbol{D} = \rho_f \,, \tag{1.2}$$

$$\nabla \times \boldsymbol{E} + \frac{\partial \boldsymbol{B}}{\partial t} = 0 \,, \tag{1.3}$$

$$\nabla \cdot \boldsymbol{B} = 0 \,. \tag{1.4}$$

We will now restrict ourselves for the purpose of this work to materials that abide by the following relations. We denote $\boldsymbol{\varepsilon}$ and $\boldsymbol{\mu}$ as tensors of relative permittivity and relative permeability, respectively. Further on we denote ε_0 and μ_0 as permittivity and permeability of vacuum. The symbol $\boldsymbol{\sigma}$ represents the tensor conductivity. The material relations are stated as follows

$$\boldsymbol{D} = \varepsilon_0 \boldsymbol{\varepsilon} \boldsymbol{E} \,, \tag{1.5}$$

$$\boldsymbol{B} = \mu_0 \boldsymbol{\mu} \boldsymbol{H} \,, \tag{1.6}$$

$$\boldsymbol{j}_f = \boldsymbol{\sigma} \boldsymbol{E} \,. \tag{1.7}$$

For further manipulations with the equations we assume that the medium is static ($\frac{\partial \boldsymbol{\varepsilon}}{\partial t}, \frac{\partial \boldsymbol{\mu}}{\partial t}, \frac{\partial \boldsymbol{\sigma}}{\partial t} = \boldsymbol{0}$). We also assume that the relative permeability is approximately equal to $\mathbf{1}$. Relative permittivity and permeability are both in general second-rank tensors but the magnetic interaction of light with a material at optical frequencies is negligible [10, 11]. This is derived from it's small effect on the spins of electrons [12] and also it's incomparable effect on the orbiting electrons relative to the electric field due to the Lorentz force.

With these assumptions we can then combine the equation (1.3) with (1.6) and the equation (1.1) with (1.5) and with (1.7) so that we arrive at the following equations

$$\frac{1}{\mu_0} \nabla \times \boldsymbol{E} + \frac{\partial \boldsymbol{H}}{\partial t} = 0\,, \tag{1.8}$$

$$\nabla \times \boldsymbol{H} - \varepsilon_0 \boldsymbol{\varepsilon} \frac{\partial \boldsymbol{E}}{\partial t} - \boldsymbol{\sigma} \boldsymbol{E} = 0\,. \tag{1.9}$$

By using a curl on the equation (1.8) and differentiation with respect to time on the equation (1.9) we get

$$\nabla \times (\frac{1}{\mu_0} \nabla \times \boldsymbol{E}) + \nabla \times \frac{\partial \boldsymbol{H}}{\partial t} = 0\,, \tag{1.10}$$

$$\nabla \times \frac{\partial \boldsymbol{H}}{\partial t} - \varepsilon_0 \boldsymbol{\varepsilon} \frac{\partial^2 \boldsymbol{E}}{\partial t^2} - \boldsymbol{\sigma} \frac{\partial \boldsymbol{E}}{\partial t} = 0\,. \tag{1.11}$$

Substituting (1.11) into (1.10) and using the identity for curl of a curl of a vector field we arrive at the final form of the electromagnetic wave equation

$$\Delta \boldsymbol{E} - \varepsilon_0 \mu_0 \boldsymbol{\varepsilon} \frac{\partial^2 \boldsymbol{E}}{\partial t^2} - \mu_0 \boldsymbol{\sigma} \frac{\partial \boldsymbol{E}}{\partial t} - \nabla(\nabla \cdot \boldsymbol{E}) = 0\,, \tag{1.12}$$

which is a linear second-order partial differential equation with respect to $\boldsymbol{E}$.

1.2   Plane wave solution in vacuum

Suppose now that we have an isotropic, homogeneous, non-conductive medium without any free current or charge, i.e. vacuum. The wave equation (1.12) is then reduced to

$$\Delta \boldsymbol{E} - \frac{1}{c^2} \frac{\partial^2 \boldsymbol{E}}{\partial t^2} = 0\,, \tag{1.13}$$

where $c = 1/\sqrt{\mu_0 \varepsilon_0}$ is the speed of light in vacuum.

A solution to this wave equation can be given in a form of a plane wave. A plane wave is such a wave that abides by $\mathbf{E}(\boldsymbol{r}, t) = \boldsymbol{E}(\boldsymbol{r} \cdot \boldsymbol{s}, t)$, where $\boldsymbol{s}$ is a unit vector in a fixed direction (generally in the direction of motion of the wave). The plane wave that we are going to be leaning heavily on in this work is a monochromatic time-harmonic plane wave given by

$$\boldsymbol{E}(\boldsymbol{r}, t) = \boldsymbol{E}_0 \cos(\omega t - \boldsymbol{k} \cdot \boldsymbol{r} + \delta) = \mathrm{Re}\Big\{\boldsymbol{E}_0 e^{i(\omega t - \boldsymbol{k} \cdot \boldsymbol{r} + \delta)}\Big\}\,, \tag{1.14}$$

where $\boldsymbol{E}_0$ is the amplitude of the wave and ω, $\boldsymbol{k}$, δ are the angular frequency, wavevector and phase shift, respectively.

2. Polarization of light

In the previous chapter we have derived the electromagnetic wave equation and we have introduced the plane wave as it's solution in vacuum. Now we will use that knowledge to approach light as a time-harmonic plane wave in order to define polarization. Moreover we will present a mathematical apparatus for describing the change in polarization for light propagating in an optical system.

2.1   Introduction

Polarization is a property of transverse waves, such as electromagnetic plane waves, describing the geometrical oscillations of, in our case, the electric field vector $\boldsymbol{E}$.

If we consider a time-harmonic monochromatic plane wave given by (1.14) we can derive that it can oscillate on any given line perpendicular to the direction of motion.

Let us now consider a more general case of polarization originating from the superposition of two time-harmonic monochromatic plane waves of the same frequency. Without loss of generality let the direction of propagation be parallel to the $\boldsymbol{z}$ axis for both waves. Also let the oscillations of one wave be parallel to the $\boldsymbol{x}$ axis and the other parallel to the $\boldsymbol{y}$ axis. We can write this superposition in terms of it's components in agreement with Maxwell's equations as

$$E_x(z,t) = E_{0x}\,\cos(\omega t - kz + \delta_x)\,, \tag{2.1}$$

$$E_y(z,t) = E_{0y}\,\cos(\omega t - kz + \delta_y)\,, \tag{2.2}$$

$$E_z(z,t) = 0\,, \tag{2.3}$$

where E_{0x}, E_{0y} are positive amplitudes of the corresponding components and δ_x, δ_y are their phase offsets. The constants ω and k are angular frequency and the magnitude of the wavevector, respectively.

If we now define $\tau := (\omega t - kz)$ and we divide the above equations by their respective amplitudes we get

$$\frac{E_x}{E_{0x}} = \cos(\tau + \delta_x) = \cos(\tau)\cos(\delta_x) - \sin(\tau)\sin(\delta_x)\,, \tag{2.4}$$

$$\frac{E_y}{E_{0y}} = \cos(\tau + \delta_y) = \cos(\tau)\cos(\delta_y) - \sin(\tau)\sin(\delta_y)\,. \tag{2.5}$$

Let us now multiply (2.4) and (2.5) by $\sin\delta_y$ and $\sin\delta_x$, respectively, and take the difference of the two. Let us also multiply (2.4) and (2.5) by $\cos\delta_y$ and $\cos\delta_x$, respectively, and then take the difference of the two. We have acquired the following set of equations

$$\frac{E_x}{E_{0x}} \sin \delta_y - \frac{E_y}{E_{0y}} \sin \delta_x = \cos(\tau) \sin(\delta_y - \delta_x)\,, \tag{2.6}$$

$$\frac{E_x}{E_{0x}} \cos \delta_y - \frac{E_y}{E_{0y}} \cos \delta_x = \sin(\tau) \sin(\delta_y - \delta_x)\,. \tag{2.7}$$

If we square both of the equations above sum them together and define $\delta := \delta_y - \delta_x$ we receive

$$\left(\frac{E_x}{E_{0x}}\right)^2 - 2\frac{E_x}{E_{0x}}\frac{E_y}{E_{0y}} \cos \delta + \left(\frac{E_y}{E_{0y}}\right)^2 = \sin^2 \delta\,. \tag{2.8}$$

What we have arrived at is the formula for an ellipse meaning that the electric field vector $\boldsymbol{E}$ traces an ellipse in the plane perpendicular to the direction of wave propagation. This ellipse of polarization (see Fig. 2.1) and hence the polarization state can be described in full by four parameters which are:

- The *azimuth θ* - an oriented angle between the positive semi axis **x** and the major axis of the ellipse. The azimuth can range from $-\pi/2$ to $\pi/2$ and determines the orientation of the ellipse.

- The *ellipticity e* - ratio of the lengths between the semi-minor axis b and the semi-major axis a of the ellipse. The ellipticity can range between -1 and 1 where it's sign is a matter of convention. In this thesis we define the negative sign to correspond to the left-hand polarization state and the positive sign to the right-hand polarization state. The handedness of the polarization represents the orientation of rotation of the electric field vector where, when looking against the propagation direction, the right-handed polarization represents a clockwise motion whereas the left-hand polarization represents a counterclockwise motion. An associated parameter ϵ defined by $\tan \epsilon = e$ is called the *ellipticity angle* and ranges between $-\pi/4$ and $\pi/4$.

- The *amplitude E_0* - measure of the overall wave amplitude. Can be given by $E_0 = \sqrt{a^2 + b^2}$ and relates to the intensity of light such that $I = E_0^2 = a^2 + b^2$.

- The *absolute phase δ_0* - an angle between the initial state of the electric field vector $\boldsymbol{E}(t = 0)$ and the **x** axis. It characterises the initial state and ranges from $-\pi$ to π.

Whilst describing the polarization state we will restrict ourselves to only the first two parameters. The amplitude carries information about the overall intensity of light which will not usually be of interest to us. More so the absolute phase which only describes the initial state and as such is not important.

We have introduced wave polarization and shown that all strictly monochromatic time-harmonic plane waves are polarized. That does not always hold true for polychromatic light. We further recognise partially polarized light and randomly polarized light. Partially polarized light is such light that changes it's polarization state randomly with time. We call the limit when the time between the changes approaches zero randomly polarized light.
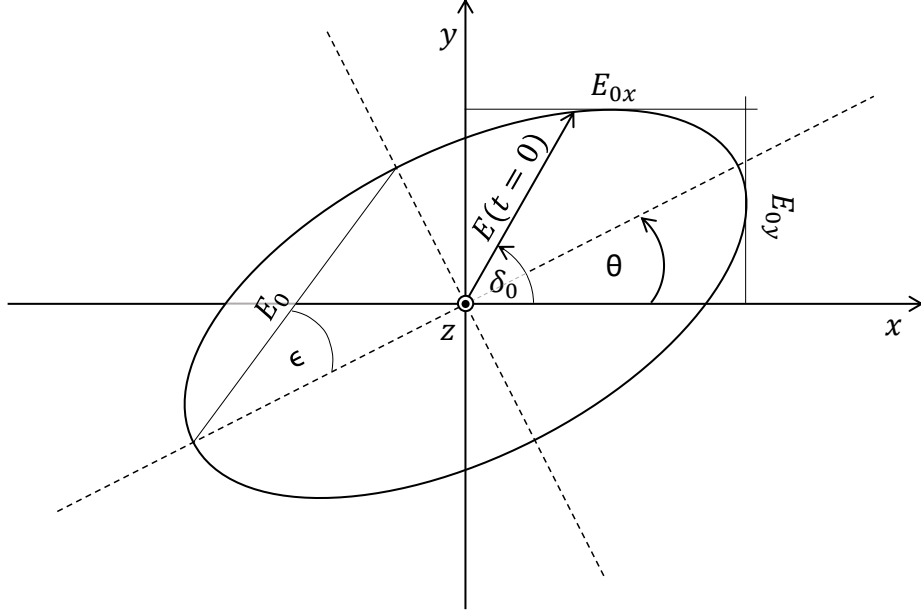
Figure 2.1: The ellipse of polarization when looking against the propagation of light.

2.2 Jones calculus

There exist several formalisms for the description of polarized light. Some of them have the advantage of also being capable to describe partially polarized light. One of the simplest, yet elegant, is the Jones formalism. The Jones formalism can be used to describe magneto-optical effects; however, it only describes fully polarized light.

2.2.1 Jones vector

The cornerstone of Jones calculus is the Jones vector. The Jones vector is defined using the complex amplitudes of a monochromatic plane wave. The complex amplitudes of a monochromatic plane wave such as the superposition of (2.1)-(2.3) are A_x and A_y defined by

$$E_x(z,t) = Re\{E_{0x}e^{i(\omega t - kz + \delta_x)}\} = Re\{A_x e^{i(\omega t - kz)}\}, \tag{2.9}$$

$$E_y(z,t) = Re\{E_{0y}e^{i(\omega t - kz + \delta_y)}\} = Re\{A_y e^{i(\omega t - kz)}\}. \tag{2.10}$$

As shown above the polarization state is fully described by four parameters. Each complex amplitude carries information about two parameters due to it's complex nature. Therefore a set of two complex amplitudes can provide complete information about the polarization state of the light wave. We use them to define the Jones vector as

$$\boldsymbol{J} = \begin{bmatrix} E_{0x}e^{i\delta_x} \\ E_{0y}e^{i\delta_y} \end{bmatrix} = \begin{bmatrix} A_x \\ A_y \end{bmatrix}, \tag{2.11}$$

which carries the complete polarization information. We generally do not need the intensity information carried by the magnitude of the complex amplitudes so

8

we normalize the Jones vector to unitary intensity. Further on we also define the parameter α using the relation $\tan \alpha = E_{0y}/E_{0x}$. Since the initial phases are not of interest to us we introduce $\delta = \delta_y - \delta_x$. Using these new parameters we can rewrite the Jones vector as

$$\boldsymbol{J} = \begin{bmatrix} \cos \alpha \\ \sin \alpha \ e^{i\delta} \end{bmatrix}. \tag{2.12}$$

The newly introduced parameters α and δ are related to the previously defined parameters θ and ϵ through the relations [13]

$$\tan 2\theta = \tan 2\alpha \cos \delta, \tag{2.13}$$

$$\sin 2\epsilon = \sin 2\alpha \sin \delta. \tag{2.14}$$

The Jones vector can be expressed in terms of any basis. The basis that we have been using so far is a Cartesian basis of linear polarizations. Another important basis is the circular polarization basis, the basis of left circular polarization (LCP) and right circular polarization (RCP). The process of switching basis is identical to that of linear algebra and can be found in [14].

- The Cartesian basis:

$$\boldsymbol{J}_x = \begin{bmatrix} 1 \\ 0 \end{bmatrix}, \ \boldsymbol{J}_y = \begin{bmatrix} 0 \\ 1 \end{bmatrix} \tag{2.15}$$

- The circular basis:

$$\boldsymbol{J}_L = \frac{1}{\sqrt{2}} \begin{bmatrix} 1 \\ -i \end{bmatrix}, \ \boldsymbol{J}_R = \frac{1}{\sqrt{2}} \begin{bmatrix} 1 \\ i \end{bmatrix} \tag{2.16}$$

In order to derive the Jones vector in terms of the azimuth θ and the ellipticity angle ϵ we utilize the rotation matrix. The rotation is in a counterclockwise direction by an arbitrary angle φ. This matrix and its inverse can also be used for the transformation of the Cartesian system. In the form written bellow this matrix represents a transformation matrix for a rotation of a Cartesian system in a clockwise direction. The rotation matrix is defined as

$$\boldsymbol{R}_T(\varphi) = \begin{bmatrix} \cos \varphi & -\sin \varphi \\ \sin \varphi & \cos \varphi \end{bmatrix}. \tag{2.17}$$

Let us now consider a polarization ellipse with the azimuth equal to zero and ellipticity angle ϵ. That means that the parameter $\alpha = \epsilon$ and $\delta = \pi/2$. Then we rotate the Cartesian system clockwise by the azimuth θ. That translates into rotating the whole ellipse in a counterclockwise direction by an azimuth θ. Such transformation of the Cartesian system is achieved using (2.17). The resulting Jones vector for general polarization in terms of θ and ϵ in the Cartesian system is

$$\boldsymbol{J}_{XY} = \begin{bmatrix} \cos \theta & -\sin \theta \\ \sin \theta & \cos \theta \end{bmatrix} \begin{bmatrix} \cos \epsilon \\ i \sin \epsilon \end{bmatrix} = \begin{bmatrix} \cos \theta \cos \epsilon - i \sin \theta \sin \epsilon \\ \sin \theta \cos \epsilon + i \cos \theta \sin \epsilon \end{bmatrix}. \tag{2.18}$$

2.2.2 Jones matrix

In this section we will show how to calculate the change of polarization upon reflection or transmission of polarized light through polarizing optical elements using the Jones calculus.

Let us have light reflecting off an optical element and two Cartesian coordinate systems $\boldsymbol{S}^{(I)}$ and $\boldsymbol{S}^{(R)}$ (see Fig. 2.2(a)) defined such that the axis $\boldsymbol{z}^{(I)}$ and $\boldsymbol{z}^{(R)}$ coincide with the wavevector before and after the reflection, respectively. The direction of the $\boldsymbol{x}$ axis is perpendicular to the plane of incidence. Light linearly polarized in this direction is called s-polarized (from German *senkrecht* - perpendicular). The direction of the $\boldsymbol{y}$ axis is parallel with the plane of incidence and light linearly polarized in its direction is called p-polarized (parallel).
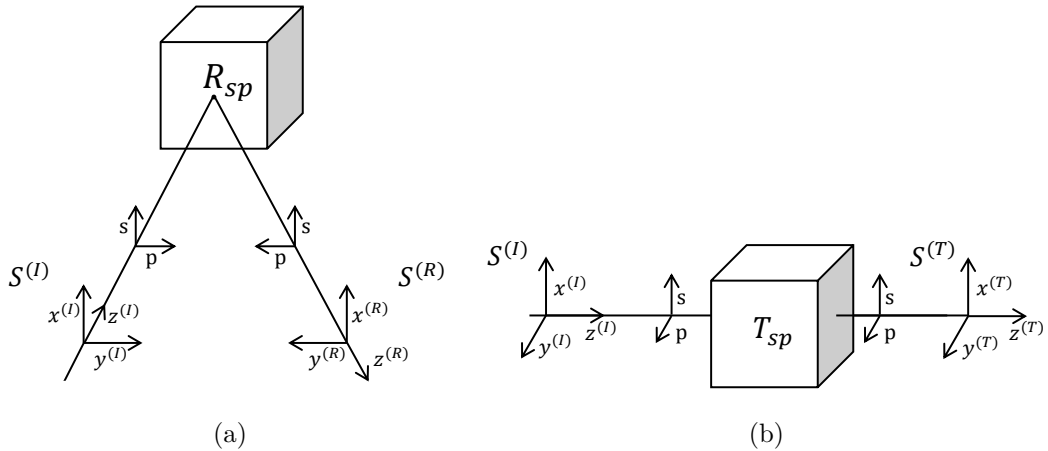

Figure 2.2: Cartesian coordinate systems for the reflection (a) and transmission (b) of light.

Let us now have the Jones vector for the incident wave in the form of $\boldsymbol{J}^{(I)}$ and the Jones vector for the reflected wave in the form of $\boldsymbol{J}^{(R)}$. The relation between the Jones vectors $\boldsymbol{J}^{(I)}$ and $\boldsymbol{J}^{(R)}$ can be then written using the Jones calculus as

$$\boldsymbol{J}^{(R)} = \boldsymbol{R}_{sp}\,\boldsymbol{J}^{(I)}, \tag{2.19}$$

where $\boldsymbol{R}_{sp}$ is the *Jones reflection matrix* of an optical element. Such matrix fully describes the effect of the optical element on the polarization state of the light wave upon reflection. We can write the reflection matrix in terms of its elements as

$$\boldsymbol{R}_{sp} = \begin{bmatrix} r_{ss} & r_{sp} \\ r_{ps} & r_{pp} \end{bmatrix}. \tag{2.20}$$

Using the definition of the Jones reflection matrix (2.19) and the definition of the Jones vector (2.11) we can write the relations between the matrix elements and the complex amplitudes of the light wave in terms of s,p-polarizations as

$$r_{ss} = \left(\frac{A_s^{(R)}}{A_s^{(I)}}\right)_{A_p^{(I)}=0}, \tag{2.21}$$

$$r_{sp} = \left(\frac{A_s^{(R)}}{A_p^{(I)}}\right)_{A_s^{(I)}=0}, \tag{2.22}$$

$$r_{ps} = \left(\frac{A_p^{(R)}}{A_s^{(I)}}\right)_{A_p^{(I)}=0}, \tag{2.23}$$

$$r_{pp} = \left(\frac{A_p^{(R)}}{A_p^{(I)}}\right)_{A_s^{(I)}=0}, \tag{2.24}$$

where the diagonal elements represent the Fresnel reflection coefficients. The off-diagonal elements represent the conversion of one polarization state to the other upon reflection.

For the case of transmission we will use the previously defined Cartesian system $\boldsymbol{S}^{(I)}$ and the s,p-polarizations. We then define the Cartesian system $\boldsymbol{S}^{(T)}$ (see Fig. 2.2(b)) such that the $\boldsymbol{z}^{(T)}$ axis is identical to $\boldsymbol{z}^{(I)}$ and the $\boldsymbol{x}^{(T)}$ and $\boldsymbol{y}^{(T)}$ axis are parallel to $\boldsymbol{x}^{(I)}$ and $\boldsymbol{y}^{(I)}$, respectively.

Let us now have the incident Jones vector $\boldsymbol{J}^{(I)}$ and the transmitted Jones vector $\boldsymbol{J}^{(T)}$. Similarly to reflection, we now define the *Jones transmission matrix* $\boldsymbol{T}_{sp}$ as

$$\boldsymbol{J}^{(T)} = \boldsymbol{T}_{sp}\,\boldsymbol{J}^{(I)}, \tag{2.25}$$

where

$$\boldsymbol{T}_{sp} = \begin{bmatrix} t_{ss} & t_{sp} \\ t_{ps} & t_{pp} \end{bmatrix}. \tag{2.26}$$

The relations between the matrix elements of the transmission matrix and the complex amplitudes of the light wave can be then written analogously to (2.21)-(2.24). With respect to the s,p-polarizations we get

$$t_{ss} = \left(\frac{A_s^{(T)}}{A_s^{(I)}}\right)_{A_p^{(I)}=0}, \tag{2.27}$$

$$t_{sp} = \left(\frac{A_s^{(T)}}{A_p^{(I)}}\right)_{A_s^{(I)}=0}, \tag{2.28}$$

$$t_{ps} = \left(\frac{A_p^{(T)}}{A_s^{(I)}}\right)_{A_p^{(I)}=0}, \tag{2.29}$$

$$t_{pp} = \left(\frac{A_p^{(T)}}{A_p^{(I)}}\right)_{A_s^{(I)}=0}. \tag{2.30}$$

So far we have shown how to model the transformation of light polarization using a single optical element in reflection or transmission. To model the entirety

of the system one must must multiply the incident Jones vector $\boldsymbol{J}^{(I)}$ by the matrices of all the optical elements in the system in their respective order. We must make sure that all the matrices are represented relative to the right coordinate system so that the transmitted (reflected) Jones vector $\boldsymbol{J}^{(T_k)}$ is represented in the same system as the incident Jones vector $\boldsymbol{J}^{(T_{k+1})}$ for the next optical element. An example of such optical system represented by optical elements with corresponding Jones matrices $\boldsymbol{X}_1, \boldsymbol{X}_2 \dots \boldsymbol{X}_N$ would be

$$\boldsymbol{J}_{out}^{(X_N)} = \boldsymbol{X}_N \boldsymbol{X}_{N-1} \dots \boldsymbol{X}_1 \boldsymbol{J}^{(I)} . \tag{2.31}$$

Lastly some of the Jones transmission matrices for the most basic optical elements are listed bellow.

<div align="center">

Cartesian basis   **Circular basis**

</div>

Linear polarizer oriented at an arbitrary angle φ with respect to the $\boldsymbol{x}$ axis

- $\boldsymbol{P}_{XY} = \begin{bmatrix} \cos^2 \varphi & \sin \varphi \cos \varphi \\ \sin \varphi \cos \varphi & \sin^2 \varphi \end{bmatrix}$ • $\boldsymbol{P}_{LR} = \frac{1}{\sqrt{2}} \begin{bmatrix} 1 & e^{2i\varphi} \\ e^{-2i\varphi} & 1 \end{bmatrix}$

Phase plate with retardance of Γ with principal axis parallel to $\boldsymbol{x}$ and $\boldsymbol{y}$

- $\boldsymbol{C}_{XY} = \begin{bmatrix} e^{i\Gamma/2} & 0 \\ 0 & e^{-i\Gamma/2} \end{bmatrix}$ • $\boldsymbol{C}_{LR} = \begin{bmatrix} \cos \frac{\Gamma}{2} & i \sin \frac{\Gamma}{2} \\ i \sin \frac{\Gamma}{2} & \cos \frac{\Gamma}{2} \end{bmatrix}$

Polarization rotator - rotating the polarization by an angle ϕ

- $\boldsymbol{N}_{XY} = \begin{bmatrix} \cos \phi & -\sin \phi \\ \sin \phi & \cos \phi \end{bmatrix}$ • $\boldsymbol{N}_{LR} = \begin{bmatrix} e^{i\phi} & 0 \\ 0 & e^{-i\phi} \end{bmatrix}$

2.3 Complex polarization parameter

Let us revisit the description of the polarization state one last time. It has been shown in the beginning of the chapter how to describe the polarization state using two parameters (θ, e) or (α, δ). In this section we introduce the *complex polarization parameter* χ defined by the ratio of the complex amplitudes as

$$\chi = \frac{A_y}{A_x} = \tan \alpha e^{i\delta} , \tag{2.32}$$

which represents another equivalent method for the description of the polarization state.

The relation of this complex parameter to the azimuth θ and the ellipticity angle ϵ can be then written for arbitrary polarization using (2.18) as

$$\chi = \frac{\sin \theta \cos \epsilon + i \cos \theta \sin \epsilon}{\cos \theta \cos \epsilon - i \sin \theta \sin \epsilon} = \frac{\tan \theta + i \tan \epsilon}{1 - i \tan \theta \tan \epsilon} . \tag{2.33}$$

Assuming small angles θ and ϵ we can approximate the tangent function by its arguments. This approximation originates from the Taylor series of the tangent

function where the first element of the series is linear. Moreover we can assume the second order term in the denominator to be zero. With these assumptions in mind we can simplify the relation (2.33) for the complex polarization parameter as

$$\chi \approx \theta + i\epsilon \,. \tag{2.34}$$

2.4 Magneto-optical observables

Magneto-optical observables are parameters describing the change in polarization upon reflection or transmission on a sample placed in a magnetic field. The case of reflection is called the magneto-optical Kerr effect (MOKE) and the case of transmission is called the magneto-optical Faraday effect. Let us consider a Cartesian basis of s and p-polarizations and an optically isotropic material. The Jones reflection matrix of such a material is diagonal indicating no transformation of an incident s-polarized wave to a reflected p-polarized wave or vice versa. However, if we introduce an anisotropy in such material the reflected light will change its polarization state. In our case the anisotropy is the result of the magnetic moment of a magnetized ferromagnetic material.

Let us consider an incident s-polarized wave impacting a magnetized ferromagnetic material. The Jones reflection matrix will no longer be diagonal and the ratio of the off-diagonal to diagonal elements of the reflection matrix for an s-polarized wave can be expressed using (2.21) and (2.23) as

$$\frac{r_{ps}}{r_{ss}} = \left(\frac{\frac{A_p^{(R)}}{A_s^{(I)}}}{\frac{A_s^{(R)}}{A_s^{(I)}}}\right)_{A_p^{(I)}=0} = \left(\frac{A_p^{(R)}}{A_s^{(R)}}\right)_{A_p^{(I)}=0} = \chi_s^{(R)} \,. \tag{2.35}$$

In our circumstances the angles $\theta_s^{(R)}$ and $\epsilon_s^{(R)}$ will always be small enough to satisfy the approximation (2.34) so that we can write

$$\chi_s^{(R)} \approx \theta_s^{(R)} + i\epsilon_s^{(R)} \,. \tag{2.36}$$

The complex magneto-optical (MO) Kerr angle Φ_{Ks} for incident s-polarization can then be defined as

$$\Phi_{Ks} := -\frac{r_{ps}}{r_{ss}} = -\chi_s^{(R)} \,, \tag{2.37}$$

$$\Phi_{Ks} \approx \theta_{Ks} - i\epsilon_{Ks} \,. \tag{2.38}$$

The above definition of the magneto-optical Kerr angle also defines two new real parameters named Kerr rotation θ_{Ks} and Kerr ellipticity ϵ_{Ks}. These parameters satisfy the following approximations

$$\theta_{Ks} \approx -\theta_s^{(R)} \tag{2.39}$$

$$\epsilon_{Ks} \approx \epsilon_s^{(R)}. \tag{2.40}$$

If we now consider the case of an incident p-polarized wave we can work analogously. With the use of (2.22) and (2.24) we get

$$\frac{r_{sp}}{r_{pp}} = \left(\frac{\frac{A_s^{(R)}}{A_p^{(I)}}}{\frac{A_p^{(R)}}{A_p^{(I)}}} \right)_{A_s^{(I)}=0} = \left(\frac{A_s^{(R)}}{A_p^{(R)}} \right)_{A_s^{(I)}=0} = (\chi_p^{(R)})^{-1}. \tag{2.41}$$

For the purpose of the p-polarized wave we need to rewrite (2.33) as

$$\chi = \frac{1 + i \cot\theta \tan\epsilon}{\cot\theta - i \tan\epsilon}. \tag{2.42}$$

The azimuth θ of the reflected p-polarized wave is not a small angle anymore as it approximately equals $\pi/2$. However, if the difference of θ and $\pi/2$ is small we can approximate the cotangent function by the first element of its Taylor series at $\pi/2$. We suppose that the tangent function of the ellipticity angle still satisfies the approximation of small angles and can be approximated by its argument. If we then assume that the second order term in the numerator is zero we get

$$\chi \approx \frac{1}{\pi/2 - \theta - i\epsilon}, \tag{2.43}$$

$$\chi^{-1} \approx \pi/2 - \theta - i\epsilon. \tag{2.44}$$

Using (2.41) we can write the definition of magneto-optical Kerr angle for an incident p-polarized wave as

$$\Phi_{Kp} := \frac{r_{sp}}{r_{pp}} = (\chi_p^{(R)})^{-1}. \tag{2.45}$$

Similar to (2.39) and (2.40) we can now define Kerr rotation and Kerr ellipticity for an incident p-polarized wave as

$$\theta_{Kp} \approx \pi/2 - \theta^{(R)}, \tag{2.46}$$

$$\epsilon_{Kp} \approx \epsilon^{(R)}. \tag{2.47}$$

This in turn allows us to write the approximation for the Kerr angle for an incident p-polarized wave in the form of

$$\Phi_{Kp} \approx \theta_{kp} - i\epsilon_{Kp}. \tag{2.48}$$

If we now go back to the definitions of the MO Kerr angle for both polarizations (2.37) and (2.45) we can explain the sign difference between them. Let's consider the case of an isotropic sample in a magnetic field. This magnetic field introduces anisotropy in the system. This anisotropy will generally result in non-zero off-diagonal elements of the reflection matrix. Let us now only consider *polar* geometry (magnetization of the sample is perpendicular to its surface). Also let the light propagate at normal incidence (angle of incidence is zero). Then from the symmetry of the problem it can be shown [15] that the elements of the Jones reflection matrix must satisfy

$$r_{ss} = -r_{pp} \,, \tag{2.49}$$

$$r_{sp} = \quad r_{ps} \,. \tag{2.50}$$

Let's now consider the MO Kerr angles in the the polar geometry at normal light incidence. Under such circumstances there is no difference between the *s,p*-polarizations since we can not define the plane of incidence. Thus we should expect the MO Kerr angles Φ_{Ks} and Φ_{Kp} to be equal. We accomplish that by the different signs in their definitions. We can verify this by using (2.49) and (2.50) in the definitions of the MO Kerr angles (2.37) and (2.45). The origin of the different signs in the definitions is then in (2.49) and is rooted in the switching of the basis upon reflection (see Fig. 2.2(a)).

3. Optically anisotropic media

This chapter begins with an introduction of the permittivity tensor. The focus is to study the permittivity tensor of a magnetized medium. Further on Yeh formalism is presented which allows for the description of light propagation in such a medium.

3.1 Permittivity tensor

The permittivity tensor ties together the material properties of the sample with the measured parameters such as the MO Kerr angle or the index of refraction. It's knowledge allows us to solve the wave equation and in turn to calculate the reflection coefficients necessary for the estimation of the MO Kerr angle. More importantly, under specific circumstances this process can be reversed, allowing us to calculate particular permittivity tensor elements from the knowledge of the MO Kerr angle.

In general, the permittivity is a second-order tensor which can be written as

$$\boldsymbol{\varepsilon} = \begin{bmatrix} \varepsilon_{xx} & \varepsilon_{xy} & \varepsilon_{xz} \\ \varepsilon_{yx} & \varepsilon_{yy} & \varepsilon_{yz} \\ \varepsilon_{zx} & \varepsilon_{zy} & \varepsilon_{zz} \end{bmatrix}. \tag{3.1}$$

External magnetic field applied to the sample may induce optical anisotropy and results in a small perturbation in it's permittivity tensor. Such perturbation can be described within the Taylor series. In this thesis we are working with the magneto-optical Kerr effect which is linear with respect to the magnetization $\boldsymbol{M}$ (magnetic dipole moment per unit volume). This approximation is justified by the small effect of the perturbation and the fact that the quadratic terms cancel out due to the nature of the measuring technique (see section 4.2). Therefore we can restrict ourselves to the first two elements of the Taylor series

$$\varepsilon_{ij} \approx \varepsilon_{ij}(0) + \left(\frac{\partial \varepsilon_{ij}}{\partial M_k} \right)_{M=0} M_k \,, \tag{3.2}$$

where the indices i,j,k each represent any index of the Cartesian basis x,y,z.

For the description of the MOKE we define three main geometrical configurations of the magnetization vector (see Fig. 3.1). In the *polar* geometry the magetization vector is perpendicular to the surface of the sample (it points along the **z** axis). In case of the *longitudinal* geometry the magnetization vector lies within the plane of incidence and also the surface plane of the sample (it points along the **y** axis). Lastly, in the *transverse* geometry the magnetization vector also lies within the surface plane; however, it is perpendicular to the plane of incidence (it points against the **x** axis).

Let us consider an optically isotropic sample placed in an external magnetic field in polar geometry. The induced magnetization introduces optical anisotropy

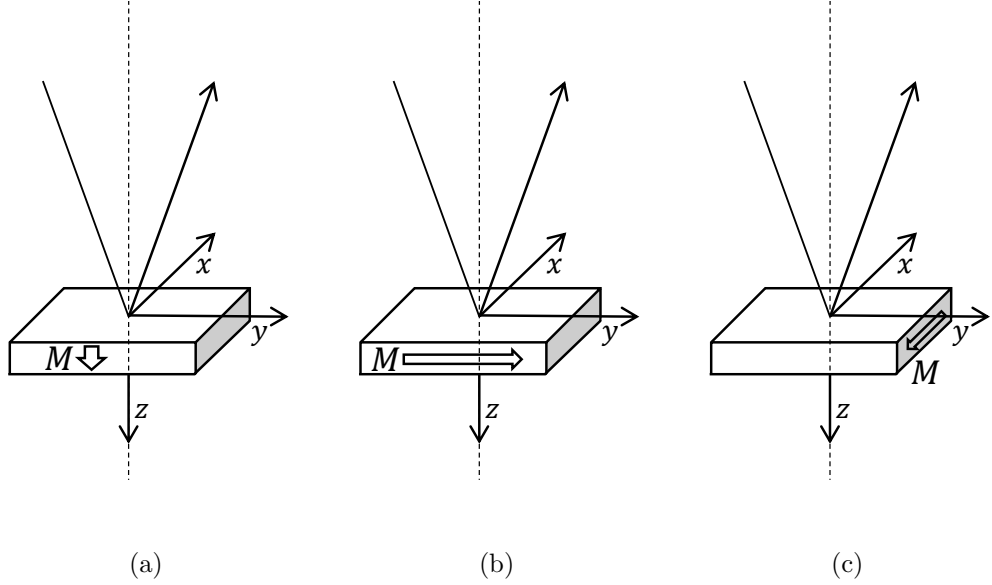(a)   (b)   (c)

Figure 3.1: Definitions of polar (a), longitudinal (b) and transversal (c) geometries for MOKE measurements for a magnetized sample.

in the system resulting in non-zero off-diagonal elements. Due to the Voigt symmetry principle [15] the permittivity tensor for such configuration must be invariant with respect to the rotation around the **z** axis. The general form of the permittivity tensor in polar configuration is then

$$\boldsymbol{\varepsilon}_p = \begin{bmatrix} \varepsilon_{xx} & \varepsilon_{xy} & 0 \\ -\varepsilon_{xy} & \varepsilon_{xx} & 0 \\ 0 & 0 & \varepsilon_{zz} \end{bmatrix} . \tag{3.3}$$

Due to our restriction to linear magneto-optical effects it can be shown [16] that $\varepsilon_{zz} \approx \varepsilon_{xx}$. Therefore we can write the permittivity tensor for polar geometry in a more conventional way as

$$\boldsymbol{\varepsilon}_p = \begin{bmatrix} \varepsilon_1 & i\varepsilon_2 & 0 \\ -i\varepsilon_2 & \varepsilon_1 & 0 \\ 0 & 0 & \varepsilon_1 \end{bmatrix} . \tag{3.4}$$

The permittivity tensor for the longitudinal geometry can then be obtained by rotating the polar coordinate system counterclockwise 90° around the **x** axis. The result of such a rotation is

$$\boldsymbol{\varepsilon}_l = \begin{bmatrix} \varepsilon_1 & 0 & i\varepsilon_2 \\ 0 & \varepsilon_1 & 0 \\ -i\varepsilon_2 & 0 & \varepsilon_1 \end{bmatrix} . \tag{3.5}$$

Analogously for the transverse geometry we carry out a counterclockwise 90° rotation around the **y** axis so that we get

$$\varepsilon_t = \begin{bmatrix} \varepsilon_1 & 0 & 0 \\ 0 & \varepsilon_1 & i\varepsilon_2 \\ 0 & -i\varepsilon_2 & \varepsilon_1 \end{bmatrix} . \tag{3.6}$$

3.2   Yeh formalism

This section introduces the formalism for the description of propagation of electromagnetic plane waves through anisotropic layered media. This formalism has been introduced in 1980 by Yeh [17] for non-absorbing materials and later extended to absorbing materials and MO effects by Višňovský [16]. The formalism relates together the electric field of the incident and the reflected or transmitted light wave. Using the knowledge of the material properties the reflection or transmission matrix, and hence the MOKE, can then be obtained allowing us to model the magneto-optic response of a layered sample.
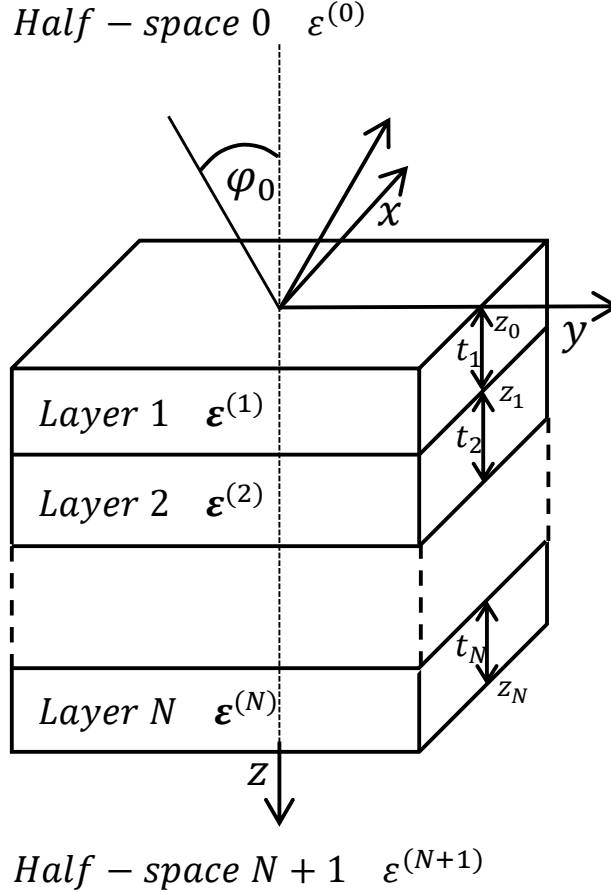
Figure 3.2: Investigated multilayer structure consisting of N anisotropic layers, with corresponding tensor permittivities $\boldsymbol{\varepsilon}^{(n)}$, surrounded by two optically isotropic half-spaces, with corresponding scalar permittivities $\varepsilon^{(0)}$ and $\varepsilon^{(N+1)}$. Each layer has a respective thickness t_n and each interface has a corresponding z_n coordinate.

Let us now consider an optically anisotropic sample consisting of *N* layers (see Fig. 3.2). These layers are mutually parallel and are perpendicular to the **z** axis. Each layer has a corresponding thickness t_n and it's optical properties are characterised by a permittivity tensor $\boldsymbol{\varepsilon}^{(n)}$. Interfaces of layers have a corresponding z_n coordinate. The layers are surrounded by half-spaces *0* and *N+1* which are isotropic and hence characterised by scalar permittivities $\varepsilon^{(0)}$ and $\varepsilon^{(N+1)}$, respectively. In this model the *N+1* half-space is an idealization of the substrate. For an incident plane wave we define a coordinate system such that the **x** axis is perpendicular to the plane of incidence and the angle of incidence is φ_0.

In order to calculate the response of the sample we will need to solve the wave equations for all the layers. Let us consider the layers to be devoid of any free current or charge. Hence, for any layer the general wave equation (1.12) can be simplified to

$$\Delta \boldsymbol{E}^{(n)} - \varepsilon_0 \mu_0 \boldsymbol{\varepsilon}^n \frac{\partial^2 \boldsymbol{E}^{(n)}}{\partial t^2} - \nabla(\nabla \cdot \boldsymbol{E}^{(n)}) = 0 \,. \tag{3.7}$$

We will now assume a solution in a form of a plane wave

$$\boldsymbol{E}^{(n)} = \boldsymbol{E}_0^{(n)} e^{i(\omega t - \boldsymbol{k}^{(n)} \cdot \boldsymbol{r})} \,. \tag{3.8}$$

The equation (3.7) can be rewritten by substituting the plane wave solution (3.8) and using the Einstein summation convention as

$$k_j^{(n)} k_j^{(n)} E_{0i}^{(n)} - k_i^{(n)} k_j^{(n)} E_{0j}^{(n)} - \frac{\omega^2}{c^2} \varepsilon_{ij}^{(n)} E_{0j}^{(n)} = 0 \,. \tag{3.9}$$

To simplify the above equation we introduce a reduced wavevector $\boldsymbol{N}$. It is a wavevector in a given medium divided by the magnitude of the wavevector in vacuum. Using a basic relation for a plane wave we can write

$$\boldsymbol{N}^{(n)} = \frac{c}{\omega} \boldsymbol{k}^{(n)} \,. \tag{3.10}$$

Our coordinate system has been chosen such that the N_x component is zero for all the layers. From the Snell's law it then follows that the N_y component is the same for all the media and is equal to

$$N_y = N_0 \sin \varphi_0 \,, \tag{3.11}$$

where N_0 is the refractive index of the front isotropic half-space. If we multiply (3.9) by $-c^2/\omega^2$ and use the reduced wavevector we get

$$N_j^{(n)} N_j^{(n)} E_{0i}^{(n)} - N_i^{(n)} N_j^{(n)} E_{0j}^{(n)} - \varepsilon_{ij}^{(n)} E_{0j}^{(n)} = 0 \,, \tag{3.12}$$

which can be written in matrix form as

$$\begin{bmatrix} \varepsilon_{xx}^{(n)} - N_y^2 - (N_z^{(n)})^2 & \varepsilon_{xy}^{(n)} & \varepsilon_{xz}^{(n)} \\ \varepsilon_{yx}^{(n)} & \varepsilon_{yy}^{(n)} - (N_z^{(n)})^2 & \varepsilon_{yz}^{(n)} + N_y N_z^{(n)} \\ \varepsilon_{zx}^{(n)} & \varepsilon_{zy}^{(n)} + N_y N_z^{(n)} & \varepsilon_{zz}^{(n)} - N_y^2 \end{bmatrix} \begin{bmatrix} E_{0x}^{(n)} \\ E_{0y}^{(n)} \\ E_{0z}^{(n)} \end{bmatrix} = 0 \,. \qquad (3.13)$$

A non-trivial solution to the above equation exists only if the determinant of the matrix is equal to zero. This leads us to the characteristic equation of the matrix which is

$$
(N_z^{(n)})^4 \varepsilon_{zz}^{(n)} +
$$
$$
+ (N_z^{(n)})^3 \left[N_y(\varepsilon_{yz}^{(n)} + \varepsilon_{zy}^{(n)}) \right] -
$$
$$
- (N_z^{(n)})^2 \left[\varepsilon_{yy}^{(n)}(\varepsilon_{zz}^{(n)} - N_y^2) + \varepsilon_{zz}^{(n)}(\varepsilon_{xx}^{(n)} - N_y^2) - \varepsilon_{xz}^{(n)}\varepsilon_{zx}^{(n)} - \varepsilon_{yz}^{(n)}\varepsilon_{zy}^{(n)} \right] -
$$
$$
- N_z^{(n)} N_y \left[(\varepsilon_{xx}^{(n)} - N_y^2)(\varepsilon_{yz}^{(n)} + \varepsilon_{zy}^{(n)}) - \varepsilon_{zx}^{(n)}\varepsilon_{xy}^{(n)} - \varepsilon_{yx}^{(n)}\varepsilon_{xz}^{(n)} \right] +
$$
$$
+ \varepsilon_{yy}^{(n)} \left[(\varepsilon_{xx}^{(n)} - N_y^2)(\varepsilon_{zz}^{(n)} - N_y^2) - \varepsilon_{xz}^{(n)}\varepsilon_{zx}^{(n)} \right] - \varepsilon_{xy}^{(n)}\varepsilon_{yx}^{(n)}(\varepsilon_{zz}^{(n)} - N_y^2) -
$$
$$
- \varepsilon_{yz}^{(n)}\varepsilon_{zy}^{(n)}(\varepsilon_{xx}^{(n)} - N_y^2) + \varepsilon_{xy}^{(n)}\varepsilon_{zx}^{(n)}\varepsilon_{yz}^{(n)} + \varepsilon_{yx}^{(n)}\varepsilon_{xz}^{(n)}\varepsilon_{zy}^{(n)} = 0 \,. \qquad (3.14)
$$

For the four roots $N_{zj}^{(n)}$ of the characteristic equation we acquire four solutions [16]

$$
\boldsymbol{e}_j^{(n)} = \begin{bmatrix} -\varepsilon_{xy}^{(n)}\left(\varepsilon_{zz}^{(n)} - N_y^2\right) + \varepsilon_{xz}^{(n)}\left(\varepsilon_{zy}^{(n)} + N_y N_{zj}^{(n)}\right) \\ \left(\varepsilon_{zz}^{(n)} - N_y^2\right)\left(\varepsilon_{xx}^{(n)} - N_y^2 - (N_{zj}^{(n)})^2\right) - \varepsilon_{xz}^{(n)}\varepsilon_{zx}^{(n)} \\ -\left(\varepsilon_{xx}^{(n)} - N_y^2 - (N_{zj}^{(n)})^2\right)\left(\varepsilon_{zy}^{(n)} + N_y N_{zj}^{(n)}\right) + \varepsilon_{xy}^{(n)}\varepsilon_{zx}^{(n)} \end{bmatrix} \,. \qquad (3.15)
$$

These solutions, also called proper modes, are polarizations left unchanged during the propagation through the corresponding medium. As the equation (3.13) is linear they can serve as a basis for the description of propagation of an arbitrary plane wave through the medium. We can then write the electric field $\boldsymbol{E}^{(n)}$ of the wave as

$$
\boldsymbol{E}^{(n)} = \sum_{j=1}^{4} E_{0j}^{(n)} \boldsymbol{e}_j^{(n)} e^{i\left\{\omega t - \frac{\omega}{c}\left[N_y y + N_{zj}^{(n)}(z - z_n)\right]\right\}} \,. \qquad (3.16)
$$

For plane waves the relation between the magnetic field and electric field follows from the Maxwell's equations as

$$
\boldsymbol{B} = \frac{1}{c}\boldsymbol{N} \times \boldsymbol{E} \,. \qquad (3.17)
$$

Using this relation we can obtain the magnetic field in terms of the proper modes as

$$\boldsymbol{B}^{(n)} = \frac{1}{c} \sum_{j=1}^{4} E_{0j}^{(n)} \boldsymbol{b}_j^{(n)} e^{i\left\{\omega t - \frac{\omega}{c}\left[N_y y + N_{zj}^{(n)}(z-z_n)\right]\right\}}, \tag{3.18}$$

where $\boldsymbol{b}_j^{(n)}$ stands for the proper magnetic modes given by

$$\boldsymbol{b}_j^{(n)} = \boldsymbol{N}_j^{(n)} \times \boldsymbol{e}_j^{(n)}. \tag{3.19}$$

Having solved the wave equation within all the layers of the sample we now have to apply the boundary conditions. From Maxwell's equation (1.3) it follows that the tangential components of the electric field vector are continuous at the interface between any two media. From Maxwell's equation (1.1) it follows that in any media without free current the tangential components of the magnetic field vector are also continuous. These requirements can be expressed for any interface as

$$\sum_{j=1}^{4} E_{0j}^{(n-1)} \boldsymbol{e}_j^{(n-1)} \cdot \boldsymbol{x} = \sum_{j=1}^{4} E_{0j}^{(n)} \boldsymbol{e}_j^{(n)} \cdot \boldsymbol{x} e^{i\frac{\omega}{c} N_{zj}^{(n)} t_n}, \tag{3.20}$$

$$\sum_{j=1}^{4} E_{0j}^{(n-1)} \boldsymbol{b}_j^{(n-1)} \cdot \boldsymbol{y} = \sum_{j=1}^{4} E_{0j}^{(n)} \boldsymbol{b}_j^{(n)} \cdot \boldsymbol{y} e^{i\frac{\omega}{c} N_{zj}^{(n)} t_n}, \tag{3.21}$$

$$\sum_{j=1}^{4} E_{0j}^{(n-1)} \boldsymbol{e}_j^{(n-1)} \cdot \boldsymbol{y} = \sum_{j=1}^{4} E_{0j}^{(n)} \boldsymbol{e}_j^{(n)} \cdot \boldsymbol{y} e^{i\frac{\omega}{c} N_{zj}^{(n)} t_n}, \tag{3.22}$$

$$\sum_{j=1}^{4} E_{0j}^{(n-1)} \boldsymbol{b}_j^{(n-1)} \cdot \boldsymbol{x} = \sum_{j=1}^{4} E_{0j}^{(n)} \boldsymbol{b}_j^{(n)} \cdot \boldsymbol{x} e^{i\frac{\omega}{c} N_{zj}^{(n)} t_n}. \tag{3.23}$$

These equations can also be written in matrix form as

$$\boldsymbol{D}^{(n-1)} \boldsymbol{E}_0^{(n-1)} = \boldsymbol{D}^{(n)} \boldsymbol{P}^{(n)} \boldsymbol{E}_0^{(n)}, \tag{3.24}$$

where we introduced the dynamical $\boldsymbol{D}^{(n)}$ matrix and the propagation $\boldsymbol{P}^{(n)}$ matrix. The dynamical matrix describes the transformation of the light wave at the interface. It can be written in terms of it's elements as

$$\boldsymbol{D}^{(n)} = \begin{bmatrix} \boldsymbol{e}_1^{(n)} \cdot \boldsymbol{x} & \boldsymbol{e}_2^{(n)} \cdot \boldsymbol{x} & \boldsymbol{e}_3^{(n)} \cdot \boldsymbol{x} & \boldsymbol{e}_4^{(n)} \cdot \boldsymbol{x} \\ \boldsymbol{b}_1^{(n)} \cdot \boldsymbol{y} & \boldsymbol{b}_2^{(n)} \cdot \boldsymbol{y} & \boldsymbol{b}_3^{(n)} \cdot \boldsymbol{y} & \boldsymbol{b}_4^{(n)} \cdot \boldsymbol{y} \\ \boldsymbol{e}_1^{(n)} \cdot \boldsymbol{y} & \boldsymbol{e}_2^{(n)} \cdot \boldsymbol{y} & \boldsymbol{e}_3^{(n)} \cdot \boldsymbol{y} & \boldsymbol{e}_4^{(n)} \cdot \boldsymbol{y} \\ \boldsymbol{b}_1^{(n)} \cdot \boldsymbol{x} & \boldsymbol{b}_2^{(n)} \cdot \boldsymbol{x} & \boldsymbol{b}_3^{(n)} \cdot \boldsymbol{x} & \boldsymbol{b}_4^{(n)} \cdot \boldsymbol{x} \end{bmatrix}. \tag{3.25}$$

The propagation matrix describes the propagation of light through the corresponding layer and is given as

$$\boldsymbol{P}^{(n)} = \begin{bmatrix} e^{i\frac{\omega}{c}N_{z1}^{(n)}t_n} & 0 & 0 & 0 \\ 0 & e^{i\frac{\omega}{c}N_{z2}^{(n)}t_n} & 0 & 0 \\ 0 & 0 & e^{i\frac{\omega}{c}N_{z3}^{(n)}t_n} & 0 \\ 0 & 0 & 0 & e^{i\frac{\omega}{c}N_{z4}^{(n)}t_n} \end{bmatrix}. \tag{3.26}$$

We can further rewrite (3.24) as

$$\boldsymbol{E}_0^{(n-1)} = (\boldsymbol{D}^{(n-1)})^{-1}\boldsymbol{D}^{(n)}\boldsymbol{P}^{(n)}\boldsymbol{E}_0^{(n)} = \boldsymbol{T}^{(n-1,n)}\boldsymbol{E}_0^{(n)}, \tag{3.27}$$

where we introduce the transfer matrix $\boldsymbol{T}^{(n-1,n)}$. It characterises the relation of the field components in two adjacent layers. This matrix can be constructed for all interfaces with the exception of the last one. Since we consider the substrate to be semi-infinite we can not write it's propagation matrix and hence we define the transfer matrix of the last interface as

$$\boldsymbol{E}_0^{(N)} = (\boldsymbol{D}^{(N)})^{-1}\boldsymbol{D}^{(N+1)}\boldsymbol{E}_0^{(N+1)} = \boldsymbol{T}^{(N,N+1)}\boldsymbol{E}_0^{(N+1)}. \tag{3.28}$$

We can now implicitly calculate the matrix $\boldsymbol{M}$ characterising the anisotropic multilayer. From (3.27) and (3.28) we acquire

$$\boldsymbol{E}_0^{(0)} = \left(\prod_{n=1}^{N+1}\boldsymbol{T}^{(n-1,n)}\right)\boldsymbol{E}_0^{(N+1)} = \boldsymbol{M}\boldsymbol{E}_0^{(N+1)}. \tag{3.29}$$

Let us now assume that the incident light wave in the front half-space can be decomposed into two orthogonal s,p-polarizations $\boldsymbol{e}_1^{(0)}$ and $\boldsymbol{e}_3^{(0)}$ with their respective amplitudes $E_{01}^{(0)}$ and $E_{03}^{(0)}$. Let us also assume that the same follows for the reflected light wave and the polarizations $\boldsymbol{e}_2^{(0)}$ and $\boldsymbol{e}_4^{(0)}$ with the amplitudes $E_{02}^{(0)}$ and $E_{04}^{(0)}$. The proper modes of the reflected light wave are equal to those of the incident light wave with the exception of the **z**-component that points in the opposite direction (unlike on Fig. 2.2(a) where the p-polarization also switches direction). If we define the proper modes for the back half-space analogously then considering there is no light source at the back half-space we get $E_{02}^{(0)} = E_{04}^{(0)} = 0$. Therefore, we can write the equation (3.29) in terms of it's elements as

$$\begin{bmatrix} E_{01}^{(0)} \\ E_{02}^{(0)} \\ E_{03}^{(0)} \\ E_{04}^{(0)} \end{bmatrix} = \begin{bmatrix} M_{11} & M_{12} & M_{13} & M_{14} \\ M_{21} & M_{22} & M_{23} & M_{24} \\ M_{31} & M_{32} & M_{33} & M_{34} \\ M_{41} & M_{42} & M_{43} & M_{44} \end{bmatrix} \begin{bmatrix} E_{01}^{(N+1)} \\ 0 \\ E_{03}^{(N+1)} \\ 0 \end{bmatrix}. \tag{3.30}$$

With the above equation we can write the reflection coefficients using their definitions (2.21) - (2.24) as

$$r_{ss} = \left(\frac{E_{02}^{(0)}}{E_{01}^{(0)}}\right)_{E_{03}^{(0)}=0} = \frac{M_{21}M_{33} - M_{23}M_{31}}{M_{11}M_{33} - M_{13}M_{31}}, \tag{3.31}$$

$$r_{sp} = \left(\frac{E_{02}^{(0)}}{E_{03}^{(0)}}\right)_{E_{01}^{(0)}=0} = \frac{M_{11}M_{23} - M_{21}M_{13}}{M_{11}M_{33} - M_{13}M_{31}}, \tag{3.32}$$

$$r_{ps} = -\left(\frac{E_{04}^{(0)}}{E_{01}^{(0)}}\right)_{E_{03}^{(0)}=0} = -\frac{M_{41}M_{33} - M_{43}M_{31}}{M_{11}M_{33} - M_{13}M_{31}}, \tag{3.33}$$

$$r_{pp} = -\left(\frac{E_{04}^{(0)}}{E_{03}^{(0)}}\right)_{E_{01}^{(0)}=0} = -\frac{M_{11}M_{43} - M_{41}M_{13}}{M_{11}M_{33} - M_{13}M_{31}}. \tag{3.34}$$

The negative signs of the last two coefficients originate from the geometry defined at the paragraph above where we have not switched the direction of the p-polarization after reflection.

Seeing as we have been able to calculate the reflection coefficients we now have all the information needed in order to calculate the MO response of an arbitrary multilayer. Moreover we can use this procedure in reverse and from the knowledge of the MO Kerr effect and the diagonal permittivity elements calculate the off-diagonal permittivity elements for any of the three geometries defined in Fig 3.1.

4. Experimental techniques

This chapter will provide a short overview of the experimental methods used in this work. First we introduce the optical method of spectroscopic ellipsometry which will allow us to calculate the diagonal permittivity tensor elements. Afterwards we present the magneto-optical Kerr spectroscopy which will allow us to measure the magneto-optical Kerr angles. Both of these methods will be leaning on the knowledge of Jones calculus introduced in the previous chapter.

4.1   Spectroscopic ellipsometry

Spectroscopic ellipsometry (SE) is an experimental technique used to analyse the optical response of a material.

A schematic sketch of a rotating compensator ellipsometry (RCE) experimental set-up can be seen in Fig 4.1. The light coming from a wide-spectrum lamp passes through a polarizer P before reflecting off the sample S. The reflected beam then passes through a rotating compensator C, an analyzer A and finally into a detector D.
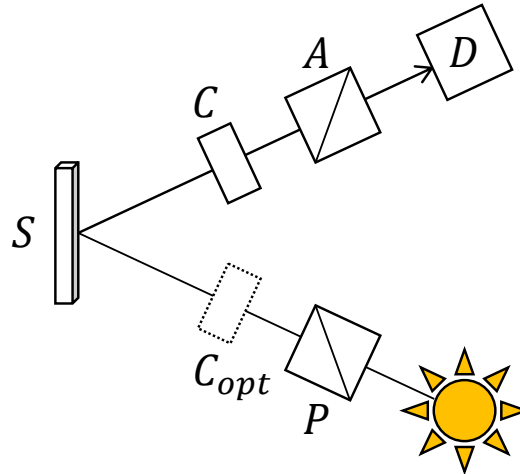
Figure 4.1: The rotating compensator ellipsometry (RCE) set-up. Light from a wide-spectrum lamp passes through a polarizer P, reflects off a sample S and continues through a rotating compensator C, analyzer A and into the detector D.

Through out this chapter we will be working in the Cartesian system with the basis of *s,p*-polarizations (see Fig. 2.2). In such a system we can use Jones formalism to calculate the resulting polarization state of the reflected light. Let us consider the polarizer P oriented at an angle ξ relative to the **s** axis. The Jones matrix corresponding to the polarizer is

$$\boldsymbol{P} = \begin{bmatrix} \cos^2 \xi & \sin \xi \cos \xi \\ \sin \xi \cos \xi & \sin^2 \xi \end{bmatrix}. \tag{4.1}$$

The Jones reflection matrix of the sample is then (2.20). However, if we consider the sample isotropic the off-diagonal elements will be zero and the resulting matrix will be

$$\boldsymbol{R} = \begin{bmatrix} r_{ss} & 0 \\ 0 & r_{pp} \end{bmatrix}. \tag{4.2}$$

The compensator is a phase plate with retardance Γ with principal axis parallel to $\boldsymbol{s}$ and $\boldsymbol{p}$ axis. Such a phase plate has a Jones transmission matrix

$$\boldsymbol{C} = \begin{bmatrix} e^{i\Gamma} & 0 \\ 0 & 1 \end{bmatrix}. \tag{4.3}$$

In this ellipsometry set-up we are using a rotating compensator. The Jones matrix of such a compensator can be derived by rotating the Cartesian system by an angle c using (2.17).

The analyzer A is a linear polarizer at an angle ζ relative to the $\mathbf{s}$ axis. Analogously to (4.1) we can write its transmission matrix as

$$\boldsymbol{A} = \begin{bmatrix} \cos^2 \zeta & \sin \zeta \cos \zeta \\ \sin \zeta \cos \zeta & \sin^2 \zeta \end{bmatrix}. \tag{4.4}$$

We can now calculate the outgoing Jones vector $\boldsymbol{J}^{(O)}$ in agreement with (2.31) as

$$\boldsymbol{J}^{(O)} = \boldsymbol{A}\boldsymbol{R}_T(c)\boldsymbol{C}\boldsymbol{R}_T(-c)\boldsymbol{R}\boldsymbol{P}\boldsymbol{J}^{(I)}. \tag{4.5}$$

From (4.5) we can determine the resulting intensity as

$$\boldsymbol{I} = (\boldsymbol{J}^{(O)})^* \boldsymbol{J}^{(O)}. \tag{4.6}$$

We are not interested in the absolute value of intensity as we have neglected it throughout the whole work. Our interest lies in the ratio of the s,p-polarizations, specifically in the ratio of r_{pp} and r_{ss} coefficients. This ratio is the defining relation for ellipsometric angles Ψ and Δ:

$$\rho = \frac{r_{pp}}{r_{ss}} = \tan \Psi e^{i\Delta}. \tag{4.7}$$

Through rotating the compensator by different angles c we can calculate Ψ and Δ from (4.6) and (4.5). We will not be showing the general case of the intensity calculation due to it's complexity but rather we will introduce a specific case. Let the polarizer P be oriented at 45 degrees and the analyzer A parallel to the $\mathbf{p}$ axis. Further more let the retardance Γ be $-\pi/2$. The negative sign means that the $\mathbf{p}$ axis is the fast axis. Then we can rewrite (4.5) as

$$\begin{bmatrix} 0 \\ J_p \end{bmatrix} = \begin{bmatrix} 0 & 0 \\ 0 & 1 \end{bmatrix} \begin{bmatrix} \cos c & -\sin c \\ \sin c & \cos c \end{bmatrix} \begin{bmatrix} -i & 0 \\ 0 & 1 \end{bmatrix} \begin{bmatrix} \cos c & \sin c \\ -\sin c & \cos c \end{bmatrix} \begin{bmatrix} \cos \Psi & 0 \\ 0 & \sin \Psi e^{i\Delta} \end{bmatrix} \begin{bmatrix} 1 \\ 1 \end{bmatrix} .$$
$$(4.8)$$

If we quantify for J_p we get

$$J_p = (\cos^2 c - i \sin^2 c) \sin \Psi e^{i\Delta} - (1 + i) \cos c \sin c \cos \Psi . \qquad (4.9)$$

We can then use the above equation and (4.6) to determine the light intensity. The full calculation can be seen in A.1.

$$I = I_0 [2 - \cos(2\Psi) - 2\sin(2\Psi)\sin(\Delta)\sin(2c) - \cos(2\Psi)\cos(4c) - \sin(2\Psi)\cos(\Delta)\sin(4c)]$$

$$I = I_0 [2 + S_1 + 2S_3 \sin(2c) + S_1 \cos(4c) - S_2 \sin(4c)] \qquad (4.10)$$

This relation allows us to measure light intensity I as a function of the angle c. We can then numerically determine the Fourier coefficients S_{1-3} and extract from them the ellipsometric angles Ψ and Δ.

For a simple bulk interface one can then calculate the index of refraction from the Fresnel reflection coefficients. In this thesis, however, we are working with thin layers deposited on a substrate. Therefore, multiple reflections within the thin layer need to be considered. For these complicated interfaces the value of the complex index of refraction is numerically modelled by a software. Typically we are investigating one layer of the sample with full knowledge of the optical and physical properties of the other layers.

If we model the complex index of refraction $\tilde{n} = n + ik$ we can then obtain the diagonal permittivity tensor element ε_1 as

$$\varepsilon_1 = \tilde{n}^2 . \qquad (4.11)$$

The introduced RCE set-up uses one compensator located after the sample reflection. For the purpose of this work the compensator could also be located before the sample reflection (see Fig. 4.1). The RC2 Woollam ellipsometer set-up used for the measurement of the ellipsometric data in Zahradník et al. [18], which are used in this work, uses both compensators. The presence of both compensators allows for the measurement of the full Mueller matrix. However, as this is not of interest to this work a simpler RCE set-up has been introduced.

4.2 Magneto-optical spectroscopy

Magneto-optical spectroscopy is a similar technique to spectroscopic ellipsometry. It allows us to measure the MO angles θ_k and ϵ_k which can be used to determine the off-diagonal tensor permittivity elements. The scheme of the experimental set-up can be seen in Fig 4.2. The main difference in MO spectroscopy is the introduction of the magnetic field making the sample optically anisotropic.

The MO spectroscopy set-up that we are using differs from the SE set-up in the rotating element. In the previous section we used a variant with a rotating compensator. For MO spectroscopy we will be using a static compensator and a rotating analyzer. Such experimental set-up can also be used for SE and it is referred to as rotating analyzer ellipsometry (RAE) with a compensator.

In the MO spectroscopy set-up we have a wide-spectrum light source emitting light that passes through a polarizer P and reflects off a sample S placed in an external magnetic field B. The reflected beam then passes through an optional compensator C, a rotating analyzer A and into a detector D. As in the previous section we can calculate the outgoing Jones vector using the Jones formalism. For the polarizer at an angle ξ we will use the transmission matrix (4.1). Analogously for the analyzer at an angle ζ we will use (4.4) and for the compensator with retardance Γ we shall use (4.3).
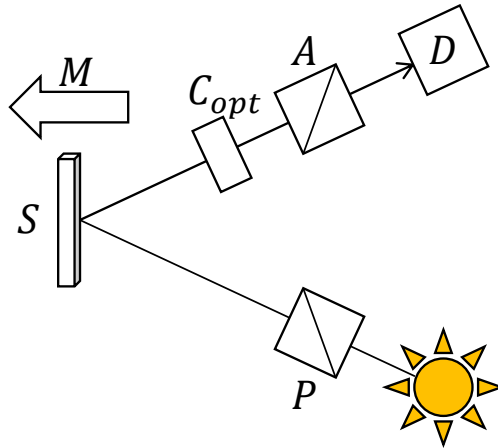
Figure 4.2: The rotating analyzer MO spectroscopy set-up. Light from a wide-spectrum lamp passes through a polarizer P, reflects off a sample S on to an optional compensator C and continues through a rotating analyzer A into the detector D.

The reflection matrix of the sample is no longer diagonal due to the anisotropy induced by the magnetic field. However, if we consider the magnetization to be in polar geometry and the angle of incidence approximately zero we can use (2.49), (2.50) and the definition of the MO Kerr angle (2.37) to write the reflection matrix (2.20) as

$$\boldsymbol{R} = \begin{bmatrix} 1 & -\Phi_k \\ -\Phi_k & -1 \end{bmatrix}. \tag{4.12}$$

In accordance with (2.31) we can then write

$$\boldsymbol{J}^{(O)} = \boldsymbol{ACSPJ}^{(I)}, \tag{4.13}$$

$$\boldsymbol{J}^{(O)} = \begin{bmatrix} \cos^2\zeta & \sin\zeta\cos\zeta \\ \sin\zeta\cos\zeta & \sin^2\zeta \end{bmatrix} \begin{bmatrix} e^{i\Gamma} & 0 \\ 0 & 1 \end{bmatrix} \begin{bmatrix} 1 & -\Phi_k \\ -\Phi_k & -1 \end{bmatrix} \begin{bmatrix} \cos^2\xi & \sin\xi\cos\xi \\ \sin\xi\cos\xi & \sin^2\xi \end{bmatrix} \boldsymbol{J}^{(I)}. \tag{4.14}$$

Let us now consider the specific case of our experimental set-up. The polarizer P is at an angle of 90° meaning that the light passing through is p-polarized. The angle of the analyzer A then also measures the angular distance from a crossed position. The resulting Jones vector for such a set-up is

$$\boldsymbol{J}^{(O)} = \begin{bmatrix} \cos^2\zeta & \sin\zeta\cos\zeta \\ \sin\zeta\cos\zeta & \sin^2\zeta \end{bmatrix} \begin{bmatrix} e^{i\Gamma} & 0 \\ 0 & 1 \end{bmatrix} \begin{bmatrix} 1 & -\Phi_k \\ -\Phi_k & -1 \end{bmatrix} \begin{bmatrix} 0 \\ 1 \end{bmatrix}, \tag{4.15}$$

$$\boldsymbol{J}^{(O)} = \begin{bmatrix} -e^{i\Gamma}\Phi_k\cos^2\zeta - \sin\zeta\cos\zeta \\ -e^{i\Gamma}\Phi_k\sin\zeta\cos\zeta - \sin^2\zeta \end{bmatrix}. \tag{4.16}$$

The intensity of the detected light can then be determined using (4.6). The full calculation can be seen in A.2 with the resulting intensity being

$$I = \sin^2\zeta + |\Phi_k|^2\cos^2\zeta + \sin(2\zeta)\,\mathrm{Re}\left\{\Phi_k e^{i\Gamma}\right\}. \tag{4.17}$$

The second order term $|\Phi_k|^2$ in the above equation can be neglected since the Kerr angle is usually a very small number (tens of millidegrees). For such an approximation the intensity in terms of the Kerr rotation θ_k and Kerr ellipticity ϵ_k can be written as

$$I = \sin^2\zeta + (\theta_k\cos\Gamma + \epsilon_k\sin\Gamma)\sin(2\zeta). \tag{4.18}$$

It is possible to measure the Kerr angle using (4.18) as a function of the angle of the analalyzer A. It is important not to forget that we have neglected the absolute value of the intensity and therefore we should introduce a multiplier I_0 on the right side of the equation. In real measurements we also introduce an additive constant I_{dark} which accounts for the dark current in the detector.

From (4.18) one can also see that for Γ equal to 0 we can directly measure the Kerr rotation. If Γ were $\pi/2$ one could also directly measure the Kerr ellipticity. The latter, unfortunately, is not possible as we are measuring a broad spectrum and there is no optical element that would act as a phase plate with retardence $\pi/2$ for all wavelengths. As such we measure the Kerr rotation directly without the compensator and then we introduce the compensator to measure the effect of both Kerr rotation and Kerr ellipticity. For each measurement we take multiple angles ζ and then fit for the measured parameter in order to improve the sensitivity.

The sensitivity is further improved by measuring the Kerr angle for both orientations of the applied magnetic field. By taking the difference of the two measurements we eliminate any unwanted optical influence and get the double Kerr angle due to the Onsager reciprocity relation [16].

5. Magnetic properties of ferromagnetic materials

Ferromagnetic materials are magnetically ordered materials whose atomic magnetic moments align within an area called a domain. For a bulk sample these domains may cancel out making the sample unmagnetized. We also call this the virgin state. However, in the presence of an external magnetic field these domains will all align in the same direction making the material magnetized. The process of alignment of the magnetic moments with respect to the external magnetic field traces a *hysteresis loop* (see Fig. 5.1). The loop is usually described using three parameters. The intrinsic spontaneous magnetization M_s, which is the saturation magnetization of the sample. An extrinsic property called the remanence magnetization M_r describing the remaining magnetization in zero external field and an extrinsic property H_c named coercivity, which describes the magnitude of the field needed to set the magnetization to zero. The two extrinsic properties depend on many extraneous factors including the shape of the sample, surface roughness, microscopic defects, thermal history and the speed at which the external field changes during the measurement [19].
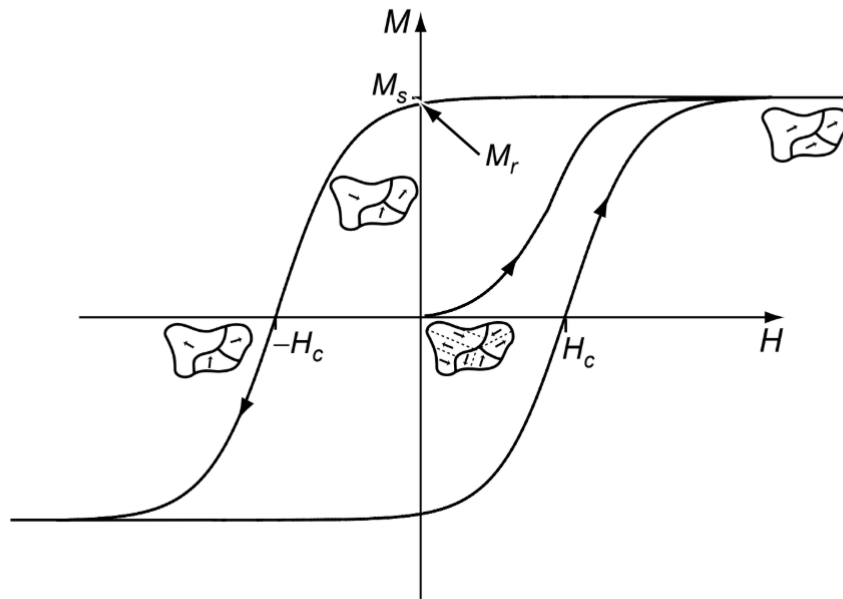
Figure 5.1: The hysteresis loop of a ferromagnetic material. Initially in an unmagnetized virgin state. With the introduction of the magnetic field H the magnetic moments of the domains begin to align until they reach the spontaneous magnetization M_s. We also recognize the remanence magnetization M_r, which remains when the applied field disappears. Lastly we denote H_c as the coercivity field needed to reduce the magnetization to zero [19].

5.1 Curie temperature

The spontaneous magnetization of a ferromagnetic material is a temperature dependent property. For every ferromagnetic material there exists a temperature, called Curie temperature T_C, at which it's spontaneous magnetization sharply falls to zero. Above this temperature the material is paramagnetic whereas bellow it, it is ferromagnetic. Above the Curie temperature the domain structure is no longer valid as the atomic magnetic moments become disordered. The temperature dependence of spontaneous magnetization of iron, cobalt and nickel can be seen on Fig. 5.2.

The relation of spontaneous magnetization and temperature can be approximated to the first order by the Bloch's law [20]

$$M_s = M_0 \left(1 - \left(\frac{T}{T_C} \right)^{3/2} \right) , \tag{5.1}$$

which holds true for low temperature measurements. For temperatures approaching the Curie temperature the spontaneous magnetization follows the dependence [20]

$$M_s \propto (T_C - T)^\beta , \tag{5.2}$$

where we introduce the critical exponent β. Combining the equations (5.1) and (5.2) we get

$$M_s = M_0 \left(1 - \left(\frac{T}{T_C} \right)^\alpha \right)^\beta . \tag{5.3}$$

This relation is used to fit the temperature dependence of the MO Kerr rotation to estimate the value of the Curie temperature for the investigated samples.
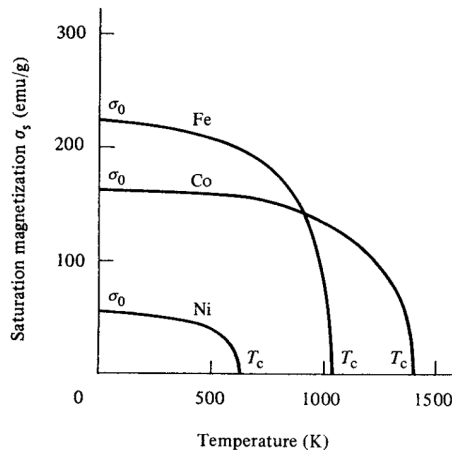
Figure 5.2: Spontaneous magnetization of iron, cobalt and nickel as a function of temperature [21].

6. Investigated samples

In this chapter, we introduce the investigated material LSMO and the deposition process used for the preparation of the samples. The samples are thin layers of LSMO deposited on four different substrates. Also introduced are the ways the epitaxial strain induced by the substrate can influence the physical properties of thin film LSMO.

6.1 Pulsed laser deposition

Pulsed laser deposition (PLD) has been one of the widely used techniques for the growth of thin films since the 1980s. A typical PLD set-up can be seen in Fig. 6.1. The material we want to deposit as a thin layer is presented as a dense target placed in a vacuum chamber. A short duration laser pulse of high energy then ablates a small part of the target creating a plasma plume. The plume reaches the substrate above it, which is usually heated to hundreds of degrees Celsius, and condensates.

If the ablation plume consists of atoms or other low-mass components it is possible to achieve epitaxial growth. Epitaxial growth is the continuation of the substrate crystallographic ordering in the deposited layer.

The investigated samples were deposited using a custom PLD set-up with a KrF laser operating at the wavelength of 248 nm. The energy fluence of the laser was 3 J/cm^2 with the repetition rate of 2 Hz. The deposition was made with the presence of background oxygen pressure of 120 mTorr whereas the postdeposition annealing process was carried out with 75 Torr of background pressure. The substrate temperature during deposition was maintained at 620 °C. The thickness of the samples is 20 nm.
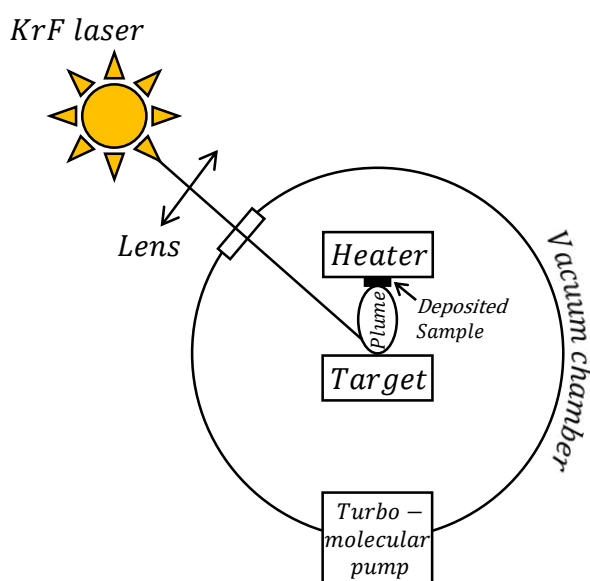
Figure 6.1: A schematic sketch of a pulsed laser deposition set-up. A high energy KrF laser impacts a dense target creating a plasma plume condensing on a substrate which is being heated to high temperatures.

6.2 La$_{2/3}$Sr$_{1/3}$MnO$_3$

The investigated samples are La$_{2/3}$Sr$_{1/3}$MnO$_3$ (LSMO) thin films deposited on different substrates. In the following paragraphs we will introduce bulk LSMO crystallography as well as the strain effects induced by the different substrates.

6.2.1 Bulk LSMO

LSMO is a member of a manganese oxide class whose ideal structure is cubic perovskite. For a general oxide ABO$_3$ the structure can be seen in Fig. 6.2. The A-site cations form the cubic cell while the B-site cation resides in it's centre surrounded by oxygen octahedron with atoms located in the centre of every face of the cube.
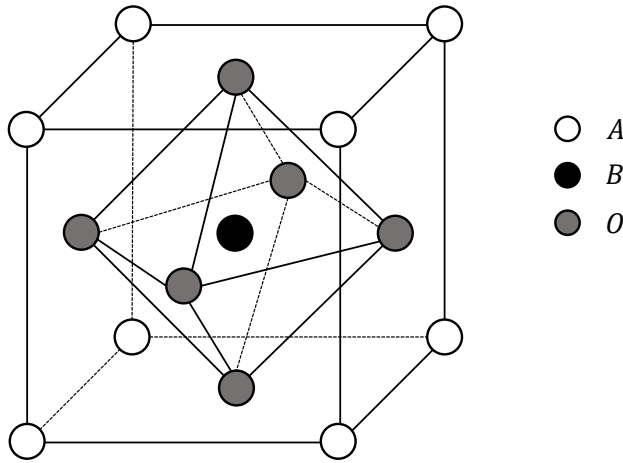
Figure 6.2: A schematic view of an ideal cubic perovskite type structure ABO$_3$.

Due to the different ionic radii of the possible cations in ABO$_3$ the structure can break the cubic symmetry and become rhombohedral or orthorhombic. Under certain circumstances the structure can also become unstable. A parameter to control the stability of the structure can be defined as

$$ t := \frac{r_A + r_O}{\sqrt{2(r_B + r_O)}} \, , \qquad (6.1) $$

where r_A, r_B and r_O are the radii of the A and B cations and oxygen, respectively. The structure can be considered stable for $0.89 < t < 1.02$ [22].

When doped by Sr the unit cell of LaMnO$_3$ becomes rhombohedral La$_{2/3}$Sr$_{1/3}$MnO$_3$ with lattice parameters $a = 5.471$ Å and $\alpha = 60.43°$ [23].

The magnetic properties of LSMO have been studied for it's irregular presence of both the Mn^{3+} and Mn^{4+} valence ions. The resulting magnetic ordering is ferromagnetic and has been explained by C. Zener [7] through the *double-exchange* (DE) interaction. In this interaction an e_g electron transfer occurs between the Mn^{3+} and Mn^{4+} valence ions through the O^{2-} 2p state (schematically shown in

Fig. 6.3). The material LSMO is a half-metal meaning that it conducts current for only one orientation of the spin and acts as an insulator for the other.

The chosen Sr doping of $La_{2/3}Sr_{1/3}MnO_3$ has been based on the work of Jonker and van Santen [5] who have found that for $La_{1-x}Sr_xMnO_3$ the doping of 1/3 provides the highest Curie temperature of about 370 K.
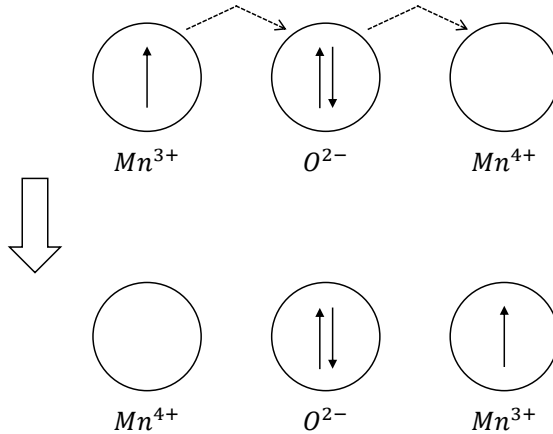
Figure 6.3: An illustration of the double-exchange interaction between the Mn^{3+} and Mn^{4+} valence ions through the O^{2-} $2p$ state in LSMO.

6.2.2 Thin film LSMO

Deposition of LSMO as a thin layer leads to certain changes in it's physical properties. Some of them arise as the effects of the epitaxial strain induced by the substrate. In order to study such effects we need to quantify the epitaxial strain. This can be done via the lattice mismatch parameter m defined as

$$m := \frac{a_l - a_s}{a_s} \,, \tag{6.2}$$

where a_l and a_s are the bulk lattice parameters of the deposited material and the substrate, respectively. If the parameter m is positive the layer is grown under compressive strain. For a negative sign the layer is grown under tensile strain.

In this work we will be examining samples with a thickness of 20 nm. Two of these samples were grown under compressive strain. The first on the diamagnetic $LaAlO_3$ (LAO) (001) oriented cubic crystal and the other on the diamagnetic $(LaAlO_3)_{1/3}(Sr_2AlTaO_6)_{2/3}$ (LSAT) (001) oriented cubic crystal. Also examined will be two samples grown under tensile strain on the diamagnetic $SrTiO_3$ (STO) in it's cubic (001) crystal orientation and on a paramagnetic $DyScO_3$ (DSO) in it's orthorhombic (110) orientation. Their lattice parameters and lattice mismatch parameters with respect to LSMO can be seen in Table 6.1 and in Fig. 6.4. For LSMO and DSO their respective pseudocubic lattice parameters are used instead.

Material	LAO	LSAT	LSMO	STO	DSO
Lattice parameter a (Å)	3.790	3.868	3.876	3.905	3.942
Lattice mismatch m (%)	2.27	0.21	-	-0.74	-1.67

Table 6.1: The cubic or pseudocubic lattice parameters for LSMO and the four substrates with corresponding lattice mismatch parameters [18, 24].
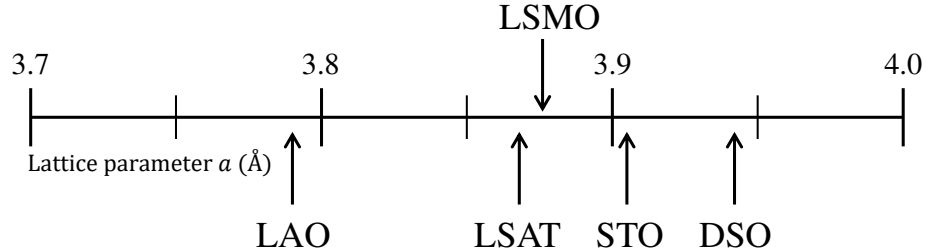
Figure 6.4: The cubic or pseudocubic lattice parameter comparison for bulk LSMO and the four substrates [18, 24].

6.2.3 Influence of epitaxial strain on physical properties

Having introduced how to quantify the epitaxial strain let us now illustrate some of it's effects.

One of the physical properties of LSMO influenced by the epitaxial strain is the orbital ordering of the manganese *3d* electron energy levels, which results in the suppression of the DE mechanism. For an isolated manganese atom the *3d* electron energy levels are all degenerated. Partial lifting of the degeneration occurs for the case of a manganese atom in a perfect perovskite type structure with the splitting of e_g and t_{2g} orbitals. Further splitting occurs as a result of lower symmetry due to the epitaxial strain and has been linked to the suppression of the DE mechanism [25].

The magnetic anisotropy of LSMO also exhibits substantial dependence on the epitaxial strain. For the bulk LSMO the easy axis of magnetization normally lies in the pseudocubic $[111]_c$ direction [26]. However, for thin films it typically moves into the plane of the film. LSMO grown under tensile strain on STO shows in-plane magnetic anisotropy. The directions $\langle 100 \rangle_c$ and $\langle 110 \rangle_c$ are equivalent easy axes of magnetization above 250K [27]. Bellow 250K the direction $\langle 110 \rangle_c$ is more pronounced [27]. LSMO thin films grown on LSAT and $NdGaO_3$ (NGO) are grown under compressive strain that is not strong enough to move the easy axis of magnetization out of the in-plane orientation. These thin films exhibit temperature dependent uniaxial and biaxial anisotropy along the $\langle 100 \rangle_c$ and $\langle 110 \rangle_c$ directions, respectively [27].

Lastly the oxygen octahedra rotations (OOR) can be induced by the epitaxial strain or the substrate symmetry. The OOR are rotations of the oxygen octahreda part of the perovskite type structure (see Fig. 6.2). Their influence on the resulting physical properties has not yet been sufficiently explained, as some, for example, claim positive correlation of the angle of the octahedral tilt and the quality of the samples magnetic properties [28] and some claim the correlation to be negative [29].

7. Strain impact on thin film La$_{2/3}$Sr$_{1/3}$MnO$_3$

The previous chapters have introduced the theory, experimental set-ups and the investigated samples. In this chapter we make use of that knowledge in order to observe the impact of strain on the electronic structure of thin film LSMO. This impact is thoroughly analysed at room temperature in the first section of this chapter. The second section aims to explore temperature dependent measurements in order to determine whether future exploration in this direction could prove noteworthy.

7.1   Room temperature MO spectroscopy

The magneto-optical Kerr effect was measured at room temperature on a home-made MO spectroscopy set-up (see Fig. 4.2). The measurement was carried out at nearly normal light incidence in a polar configuration at 1T, which at room temperature is a sufficient field for the magnetic saturation of all the samples [25]. The spectral range of the measurement was from 1.5 eV to 5 eV.

The measured spectra of the MO Kerr rotation and ellipticity can be seen on Fig. 7.2. The spectra of LSMO/DSO and LSMO/LAO have been multiplied tenfold for better clarity. For all samples the Kerr rotation spectra are dominated by a global minimum at around 3.6 eV. Also common for all samples is the local maximum at around 2.4 eV in the Kerr rotation spectra. The Kerr ellipticity spectra have an inflection point at around 3.6 eV, common to all samples, with the maximum and minimum of around 3 eV and 4 eV, respectively. The MOKE spectra are very similar in spectral shape for all samples with the exception of LSMO deposited on STO, which is influenced by the high reflectivity of STO in the UV region [1]. The amplitude of the measured MOKE shows a strong suppression of the ferromagnetic ordering for samples with higher lattice mismatch and therefore higher epitaxial strain.

Using the MOKE spectra we can numerically calculate the off-diagonal elements of the permittivity tensor of the investigated samples. The numeric calculation is based on the Yeh formalism presented in section 3.2. From there the calculation of the MOKE effect in polar configuration is based solely on known properties and the off-diagonal elements of the permittivity tensor. Therefore, we can numerically calculate the off-diagonal elements of the permittivity tensor through finding the tenser elements minimizing the difference of the measured MOKE and the calculated MOKE. The physical properties of the very same samples and the spectroscopic ellipsometry data necessary for this calculation are taken from [18].

The calculated spectra of the off-diagonal elements of the permittivity tensor can be seen on Fig 7.3. The spectra of the LSMO/DSO sample have been calculated only within the spectral range of 2 - 5 eV due to the small effect and high noise in the IR region. For all samples the spectral shape is dominated by the spectroscopic structure situated near 3.6 eV. This structure manifests itself as a

global minimum in the real part of ε_2 and as an "S" shape centred around 3.6 eV in the imaginary part. The associated electronic transition has already been reported in single crystalline thin films of LSMO grown on STO [30]. It has been characterized as a charge transfer diamagnetic transition from O $2p$ to Mn t_{2g} state in the minority spin channel (see Fig. 7.1). Another prominent transition occurs at around 2.4 eV and manifests itself most visibly as the "S" shape in the real part of the off-diagonal permittivity tensor elements. This transition has also already been reported, most notably on STO in [30], and has been characterized as a paramagnetic electronic transition from Mn t_{2g} to Mn e_g state in the majority spin channel. These transitions are also visible on the Kerr effect spectra. They are also sufficient for the description of the off-diagonal elements for the LSMO/STO and LSMO/DSO samples, that have been grown under tensile strain.
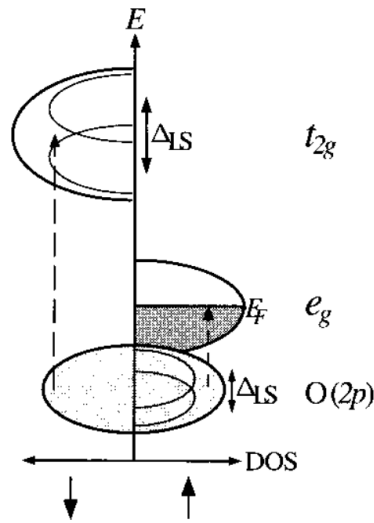
Figure 7.1: Energy-level diagram for the ground state of LSMO. Up-spin corresponds to the majority-spin states. Dashed arrows represent diamagnetic charge transfer transitions. The transition in the minority spin channel from O $2p$ to Mn t_{2g} state has been used for the interpretation of the spectral structure in the MOKE spectra of LSMO at around 3.6 eV [31].

In case of the compressively strained LSMO/LAO and LSMO/LSAT another transition has been observed in the off-diagonal elements spectra at around 4.3 eV. It can be observed in the real part of ε_2 as a small "S" shape and in the imaginary part as a change in concavity. It's effect is very small, and, therefore, not well observable in the MOKE spectra. Arguably in the Kerr rotation spectra around 4.3 eV we can see the LSMO/DSO crossing the zero line, whereas the samples grown under compressive strain (i.e. LSMO/LAO and LSMO/LSAT) show a decrease in the gradient of Kerr rotation and we do not observe the spectra crossing the zero line. In contrast to these measurements the Kerr spectra of LSMO/STO are markedly different around 3.6 eV owing to the optical contribution of STO. In the UV region the penetration depth of LSMO is high as is the reflectivity of STO [1]. Therefore, it is necessary to draw conclusions from the spectra of the off-diagonal permittivity tensor elements, where such contribution is separated.

The origin of the transition at 4.3 eV on samples grown under compressive strain has not been fully explained yet. The transition has also been observed at low temperatures on samples grown on STO under tensile strain [2]. That has lead Zahradník et al. [18] to believe that this transition is paramagnetic in nature and originates in Mn t_{2g} levels in the majority spin channel. Therefore, it is dependent on both the epitaxial strain and temperature.

From the low temperature measurements on STO [2] we can also conclude that the OOR is not the main cause of the transition at 4.3 eV. The change of temperature does not induce structural alterations large enough to influence the octahedra tilt system [25]. With the OOR remaining unchanged with temperature during the introduction of the third transition we can conclude that it does not have significant influence on the magneto-optical properties of LSMO.
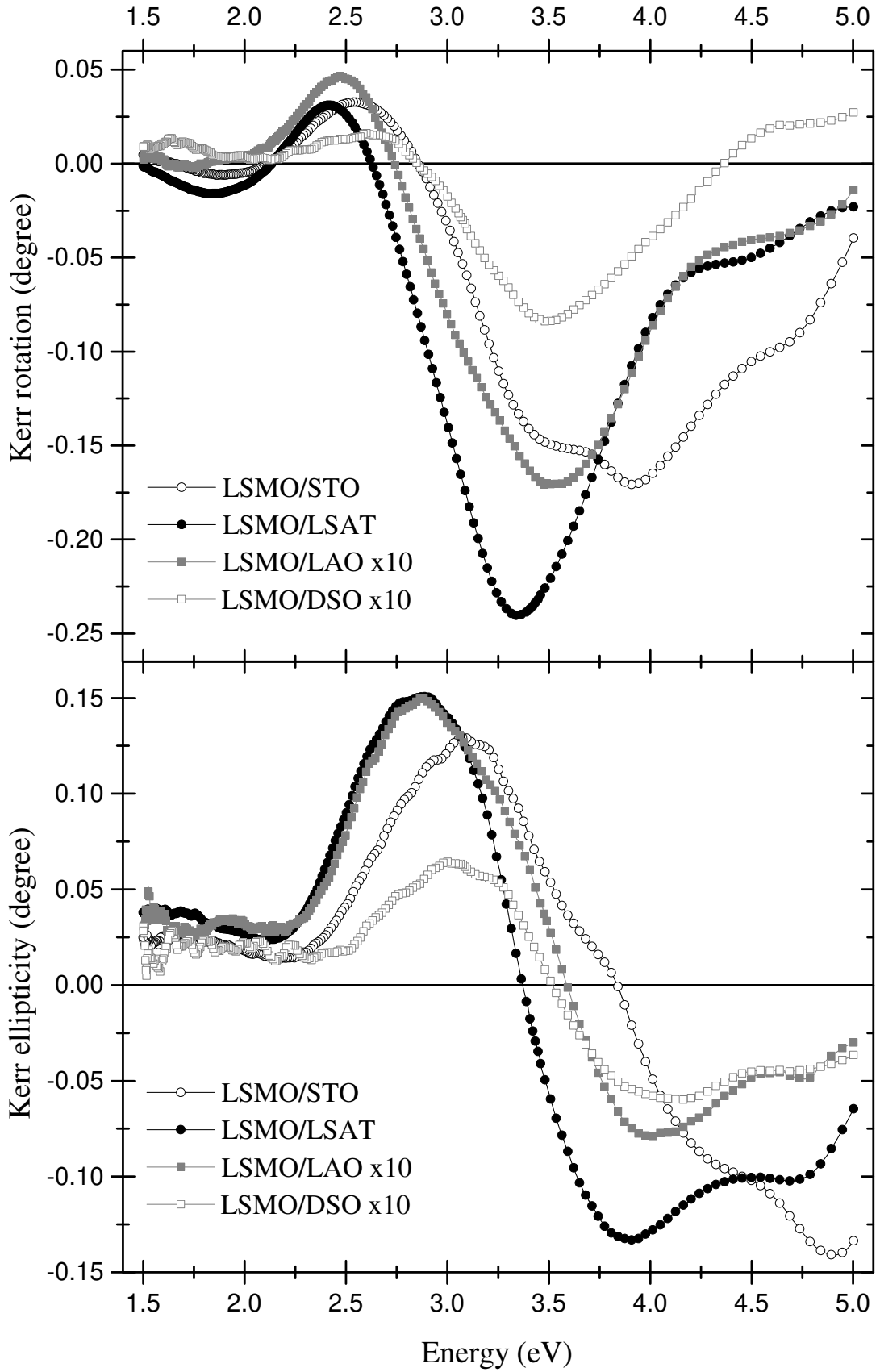
Figure 7.2: The real part (top panel) and the opposite of the imaginary part (bottom panel) of the magneto-optical Kerr effect in polar geometry of the four LSMO samples deposited on different substrates. For better clarity the spectra of the LSMO/LAO and LSMO/DSO samples have been multiplied tenfold.
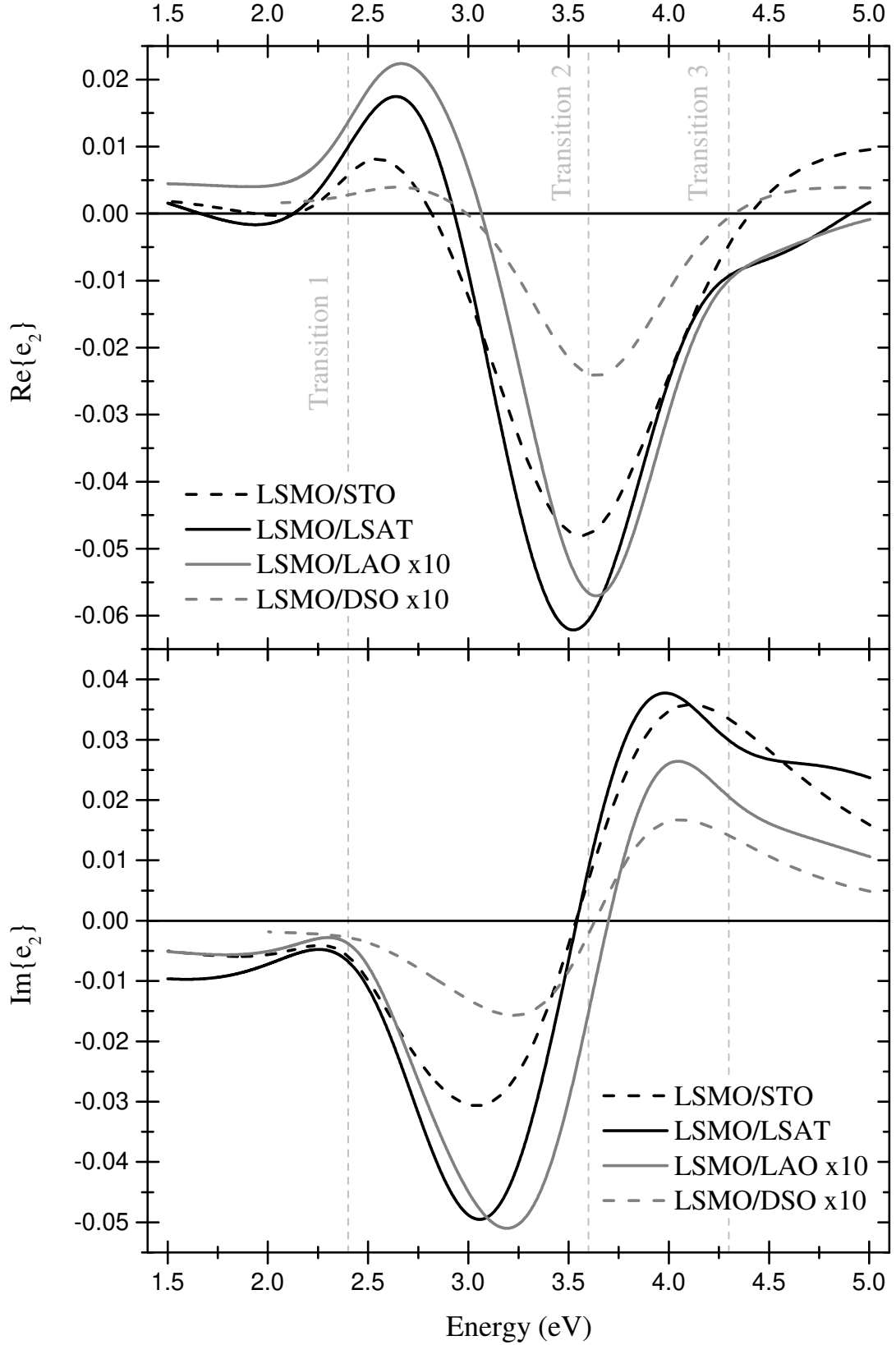
Figure 7.3: The real part (top panel) and the imaginary part (bottom panel) of the off-diagonal permittivity tensor elements of the four LSMO samples deposited on different substrates. For better clarity the spectra of the LSMO/LAO and LSMO/DSO samples have been multiplied tenfold. The vertical lines represent the approximate locations of the transitions.

7.2 Temperature dependent MO spectroscopy

Temperature dependent magneto-optical spectroscopy has been measured on a homemade set-up similar to Fig. 4.2 with the notable addition of a closed cycle helium optical cryostat around the sample. The cryostat does not allow for the placement of an electromagnet in the vicinity of the sample. Therefore, a permanent neodymium $Nd_2Fe_{14}B$ magnet attached to the back of the sample has been used. This section does not aim to provide conclusive proof and serves as a means to determine whether future exploration in this direction could prove noteworthy. We currently have no possibility of calculating the permittivity tensor elements due to the lack of temperature dependent ellipsometric measurements. Hence, only the real part of the MOKE has been measured for all four samples.

The use of a permanent magnet introduces several difficulties. It does not allow for the measurement of the difference of the MOKE for a positive and a negative field (see section 4.2). Hence, the quadratic term in the Taylor series (3.2) does not cancel out. The resulting measurement is then a combination of the linear and quadratic term. Due to the small magnitude of the effect we neglect the influence of the quadratic term. The measurement in only one polarity of the field is also more prone to errors that are optical in nature and that do not cancel out.

The placement of the permanent magnet inside the cryostat also presents difficulties. It is necessary to consider the temperature dependent magnetic properties of the magnet when evaluating the measured spectra. The T_C of neodymium magnets is around 580 K [32]. That is well above 350 K, the maximum measured temperature in this work. However, irreversible loss of magnetization can occur during prolonged sessions of temperatures higher than 350 K. No such loss of magnetization has been observed during the measurement. For neodymium magnets at the temperature of 135 K [33] a spin reorientation transition occurs. This transition is from a uniaxial material to an easy-cone material with a canting angle of no more than 30° [34]. This reversible transition results in a loss of magnetic field strength in the out-of-plane direction. The magnetic field as a function of temperature can be seen on Fig. 7.4.

The magnetic field of the neodymium magnet used in the experiments is 200 mT at room temperature. Such field is not high enough to saturate the magnetization of the measured samples [25]. This results in the suppression of magnitude of the MOKE as it is approximately linear with magnetization.

The addition of the cryostat in combination with the magnetic field also introduces the Faraday effect of the fused silica optical window. The Faraday effect is not constant across the spectrum. For the fused silica optical window this effect is concave up with a growing gradient towards the UV region and is positive.
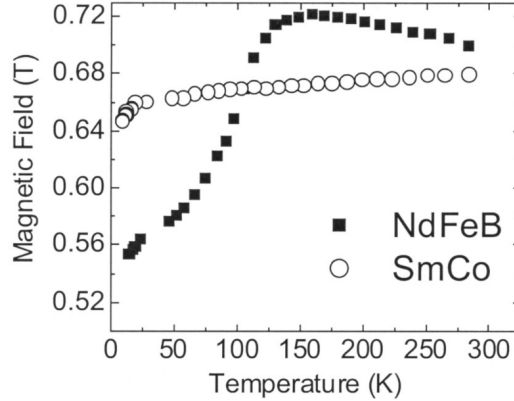
Figure 7.4: Magnetic field of NdFeB and SmCo permanent magnets as a function of temperature [33].

7.2.1 LSMO/LSAT

The measured Kerr rotation spectra of LSMO/LSAT can be seen on Fig. 7.5. The influence of the Faraday effect of the window is clearly visible as the measured spectra exceed the zero position in the UV region in contrast to the room temperature measurements on Fig. 7.2. This effect is not negligible yet it does not prevent the analysis of the spectra.

We can see that the amplitude of the spectra scales with temperature. The scaling is as to be expected, with respect to the reported temperature dependent magnetic properties of LSMO, with the notable exception of the measurements with the two lowest temperatures. The 100 K measurement notably differs in magnitude and partially in spectral shape. The difference in magnitude is most likely due to the neodymium magnet (see Fig. 7.4). The reported transition of the magnet is at 135 K. As the 100 K measurement was the first to be carried out the magnet could have retained a slightly higher temperature than the sample and therefore would have retained it's stronger magnetic properties. When the sample was cooled to 50 K the magnet passed through the spin reorientation transition, loosing some of it's magnetic field and thus causing lower overall measured effect of the sample.

The difference in spectral shape of the 100 K measurement is possibly caused by the additional transition at 4.3 eV. If the transition is truly paramagnetic in nature then it should be dependent on temperature [35]. This prominent difference is also magnified by the magnitude of the external magnetic field which is at it's maximum for the 100 K measurement.

The Curie temperature of LSMO/LSAT can be estimated by fitting the temperature dependent Kerr rotation using the function (5.3). As Kerr rotation is spectrally dependent we fit the average of the absolute values of Kerr rotation in the spectral region of 2 - 4 eV. This region has been chosen due to it's lower noise, lower Faraday effect impact of the windows and overall higher Kerr rotation. The average of the Kerr effect as a function of temperature and the numeric fit can be seen on Fig. 7.6. The approximated T_C is 356 K which is in good agreement with the T_C of 361 K measured in [25], considering the limited data and the negative influence of the temperature dependent external magnetic field.
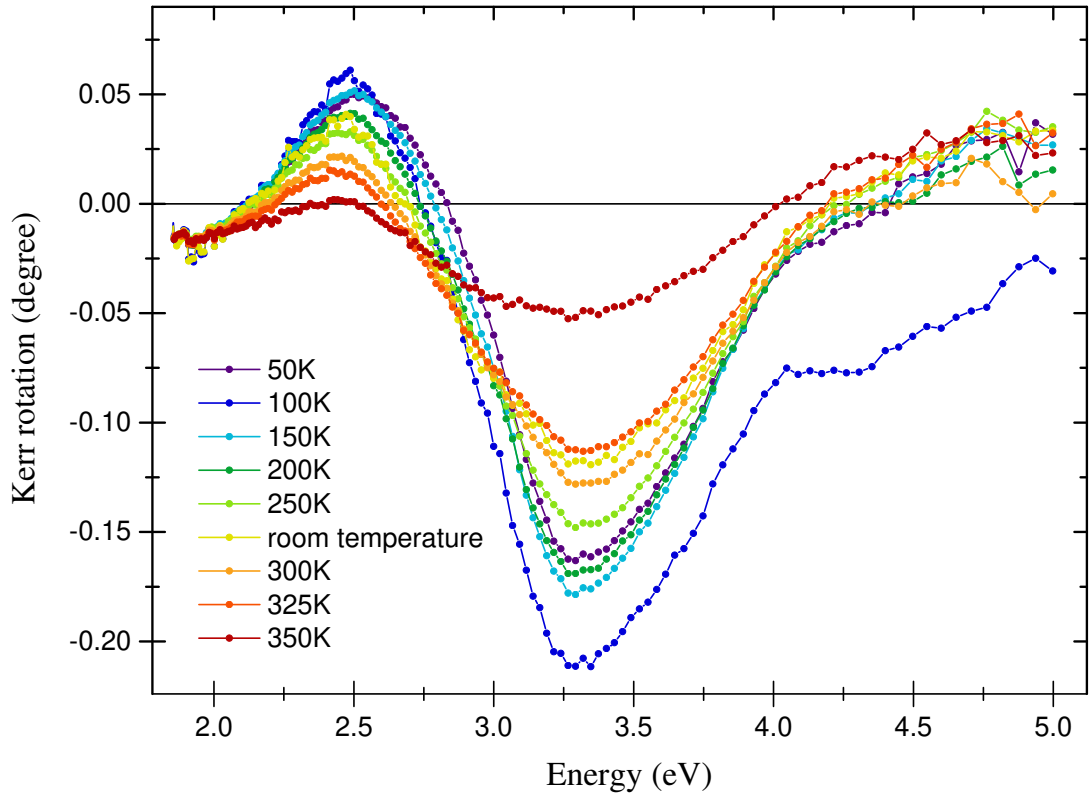
Figure 7.5: Kerr rotation spectra of LSMO/LSAT plotted for a wide range of temperatures.
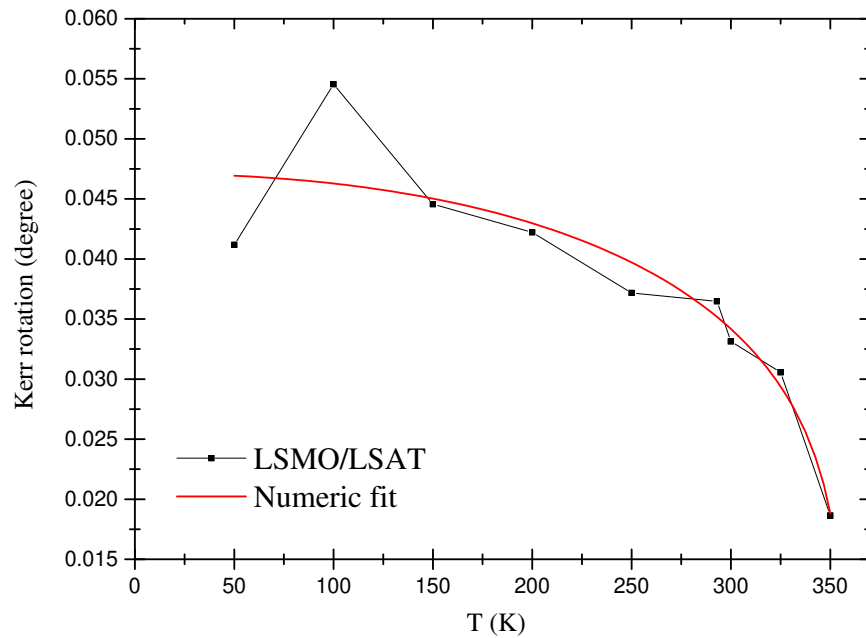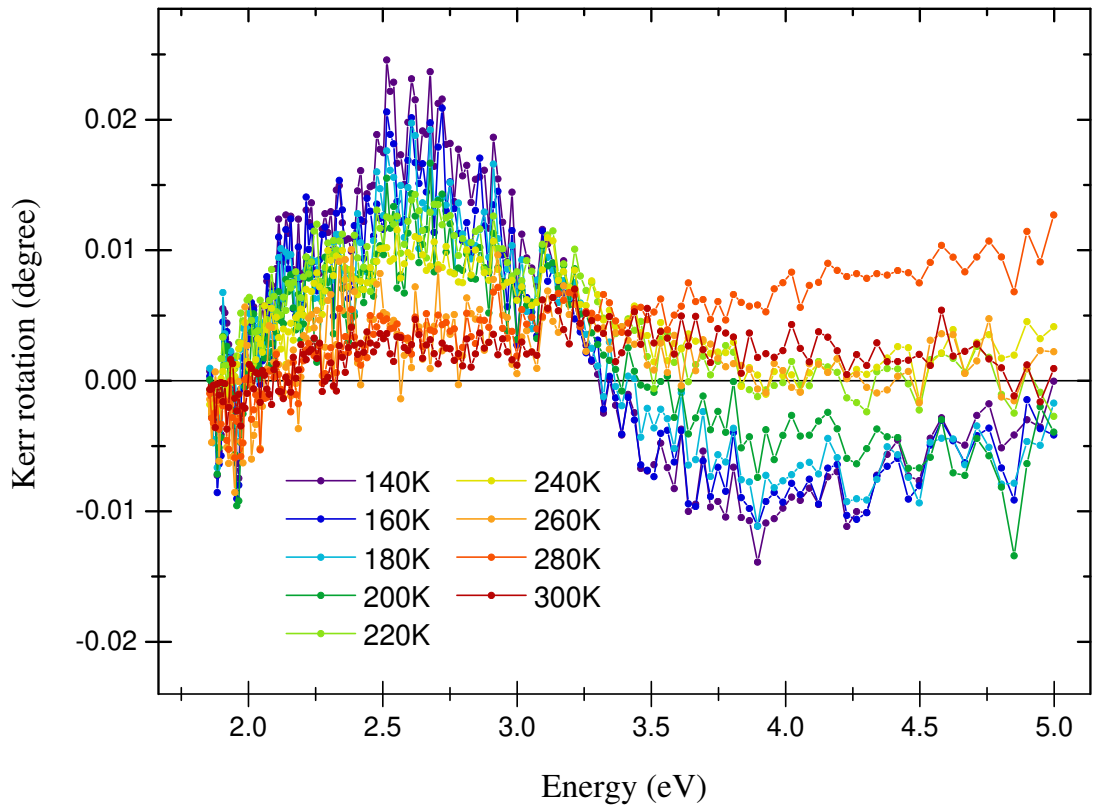

Figure 7.6: The average of the absolute values of Kerr rotation of LSMO/LSAT between 2 - 4 eV as a function of temperature. Experimentally obtained data are fitted with a theoretical model. The theoretical model gives a Curie temperature of 356 K.

7.2.2 LSMO/LAO

The measured Kerr rotation as a function of energy for LSMO/LAO can be seen on Fig. 7.7. The Faraday effect of the windows is well observable on this set of measurements as the effect of LSMO/LAO is very low at room temperature. Also well observable is the transition at 4.3 eV. The transition is more pronounced at lower temperatures further proving it to be paramagnetic.

The temperature dependent measurements of the Kerr rotation on LSMO/LAO show more substantial differences in the overall magnitudes then those of LSMO/LSAT or LSMO/STO. That is due to the fact that the magnetization of LSMO/LAO saturates at about 0.5 T whereas for LSMO/LSAT and LSMO/STO saturation occurs at around 0.2 T [25]. Therefore, the changes of the applied magnetic field with temperature impact the amplitude of LSMO/LAO more substantially.

The observed magnitudes of the Kerr rotation for low temperatures are much higher than that of LSMO/LSAT and LSMO/STO. That is in contrast with room temperature measurements (see Fig. 7.2). The lower effect at room temperature is caused by the lower Curie temperature of LSMO/LAO with respect to higher epitaxial strain. Unfortunately we are not able to fit the data and estimate the Curie temperature due to the temperature dependence of the applied magnetic field and the spin reorientation transition of LSMO/LAO occurring at 200 K [25].
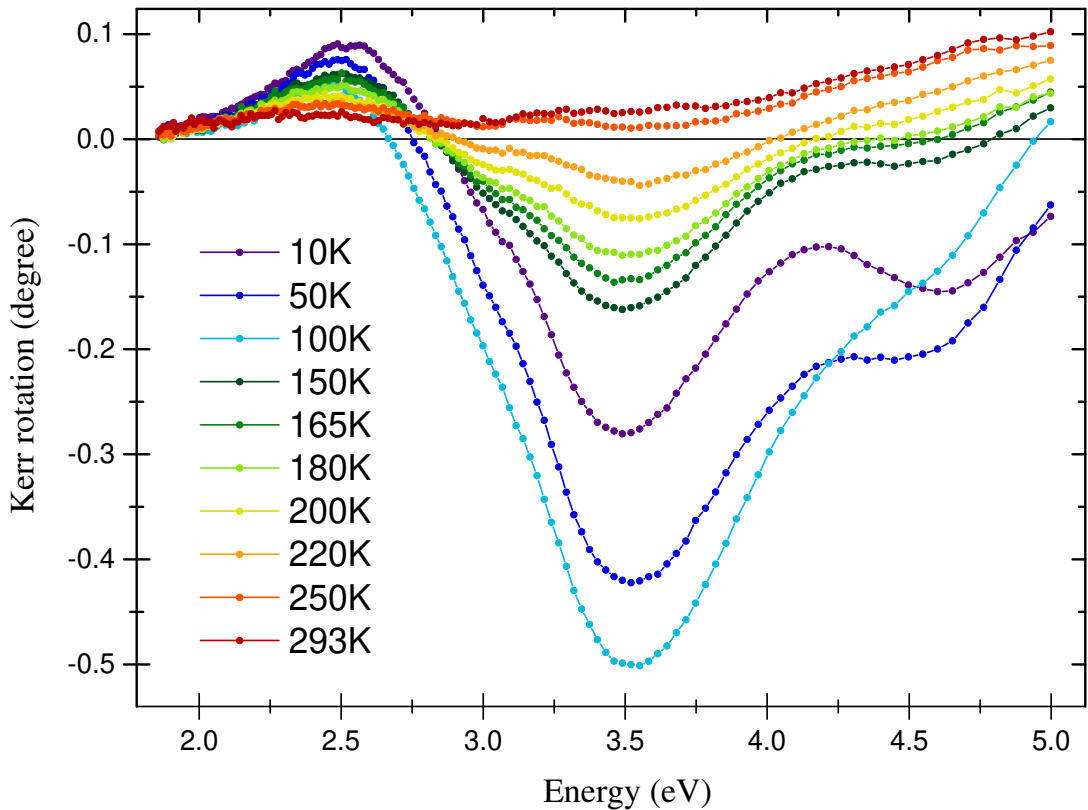
Figure 7.7: Kerr rotation spectra of LSMO/LAO plotted for a wide range of temperatures.

7.2.3 LSMO/DSO

The sample of thin film LSMO on the DSO substrate has a very small effect across all the measured temperatures (see Fig. 7.8). Therefore, the undesirable Faraday effect has a substantial influence on the measured spectra. In order to eliminate this effect Kerr rotation has been measured at the temperature of 340K where the sample showed paramagnetic behaviour. Hence, the measured effect at 340 K was solely due to the Faraday effect and optical imperfections. Therefore, this effect has then been subtracted from the measured spectra, resulting in almost pure MOKE signal. As the field of the permanent magnet is temperature dependent the Faraday effect in the optical windows at 340 K is weaker than that at lower temperatures, which leaves a small contribution in the displayed spectra.

The resulting spectra have a high level of noise. No spectral change with temperature can be observed. The magnitude does scale with temperature (see Fig. 7.9); however, the average of the absolute Kerr effects between 2 - 4 eV does not exactly follow the theoretical model. That is due to the high noise of the measurement and small MO effect of the sample. The measurement error of our set-up under perfect circumstances is lower than 1 millidegree. However, the temperature dependent measurements have a much higher error. The measurement of LSMO/DSO has an effect so small that we are on the limit of usability of this set-up. Nonetheless, when averaged out the Kerr rotation can still be fitted using the relation (5.3). This model gives the Curie temperature of 313 K. Due to the paramagnetic nature of DSO the Curie temperature of LSMO/DSO can not be determined using standard magnetometry measurements. Therefore, the successful use of the surface method of Kerr rotation for the ascertainment of the Curie temperature of LSMO/DSO is an important step.

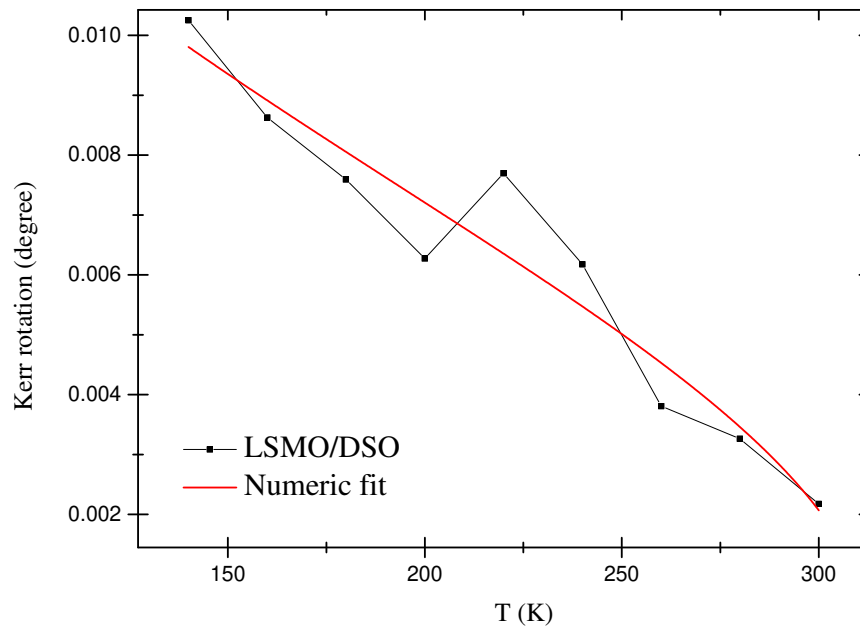Figure 7.8: Kerr rotation spectra of LSMO/DSO plotted for a wide range of temperatures.

Figure 7.9: The average of the absolute values of Kerr rotation of LSMO/DSO between 2 - 4 eV as a function of temperature. Experimentally obtained data are fitted with a theoretical model. The theoretical model gives a Curie temperature of 313 K.

7.2.4 LSMO/STO

Kerr rotation spectra of LSMO deposited on the STO substrate have been measured for multiple temperatures between 10 K and 350 K. The sample has been characterised as paramagnetic at 350 K. This is also supported by literature [25]. The measured Kerr rotation of the sample at 350 K is then solely due to the Faraday rotation of the window and optical imperfections. Therefore, as with LSMO deposited on DSO, this measurement was subtracted from the Kerr rotation spectra, thus diminishing the systematic error of the set-up. The resulting Kerr rotation spectra of LSMO deposited on STO can be seen on Fig. 7.10.

The STO substrate undergoes a structural transition at around 110 K [36] from cubic (above 110 K) to tetragonal (65 - 110 K) state. This transition changes the epitaxial strain induced on the thin film of LSMO. In the measured spectra we observe this transition as a change in the ratio of the magnitudes of the two minima peaks around 3.6 eV. Bellow 90 K the second peak has a higher magnitude. At 90 K and above we observe that the first peak has a higher amplitude. This holds true until about 150 K where we, in agreement with the room temperature measurements, observe that the second peak has a higher amplitude. This change in spectral shape is the direct result of the change of the epitaxial strain caused by the structural transition of the substrate.

The measurements at 10 K and 50 K differ in the UV part of the spectra from the other measurements. This may be due to additional structural transitions of STO. It has been observed [36] that STO changes it's structure to orthorombic bellow 65 K and to be "possibly rhombohedral" [36] at 10 K. This spectral change may also be the result of the transition at around 4.3 eV, which was previously observed on the compressively strained samples. However, our set-up does have a high noise to signal ratio above 4.5 eV and the temperature stability of the 10 K measurement was not very good in part due to the large magnet attached to the back of the sample. Therefore, this observation can not be passed as conclusive.

We have observed changes in the Kerr rotation spectra of LSMO deposited on STO at temperatures around that of the structural transition of STO. Unfortunately we are unable to comment on the effect this transition has on the magnitude of the Kerr rotation. That is due to the transition being in the temperature region with the highest changes of the applied magnetic field due to the magnet's temperature dependence (see Fig. 7.4). However, for temperatures above 150 K the changes in the magnetic field are much smaller allowing us to fit the temperature dependence of the magnitude of the Kerr rotation. The numeric fit of the average of the absolute values of the Kerr rotation between 2.5 - 4 eV gives the Curie temperature of 330 K. The temperature dependence of the magnitude of Kerr rotation can be seen on Fig. 7.11.
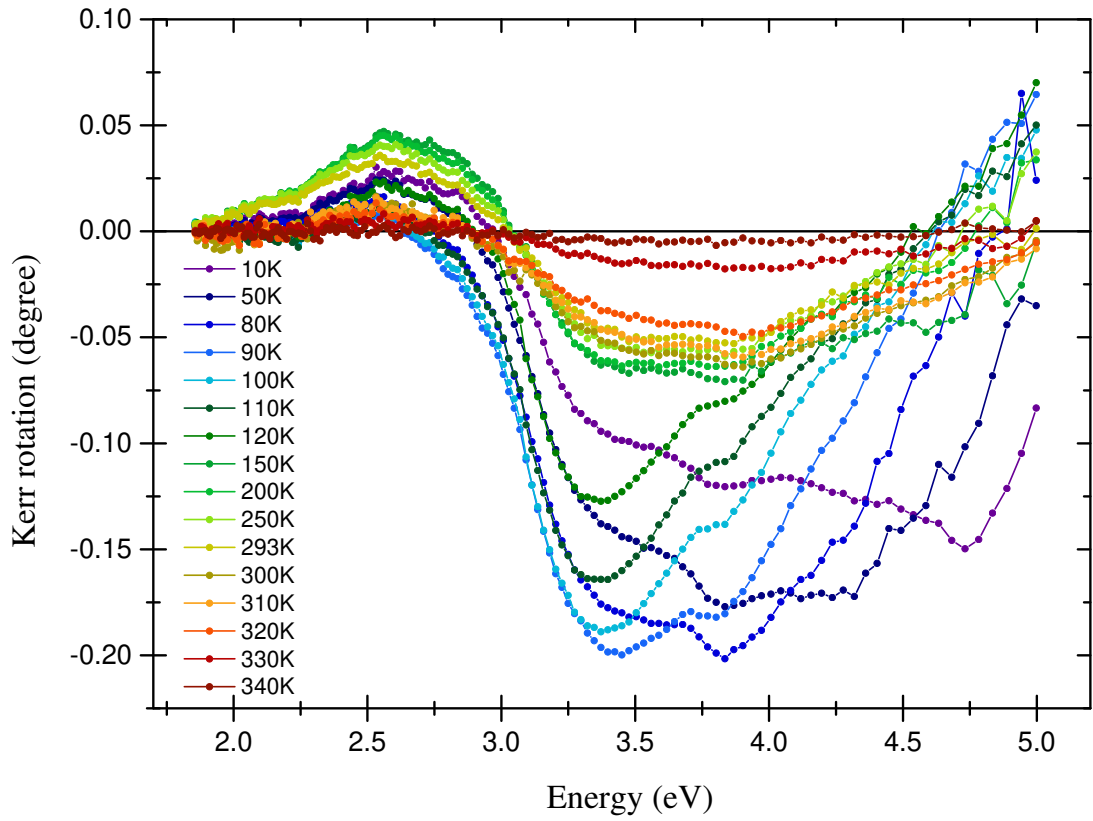
Figure 7.10: Kerr rotation spectra of LSMO/STO plotted for a wide range of temperatures.
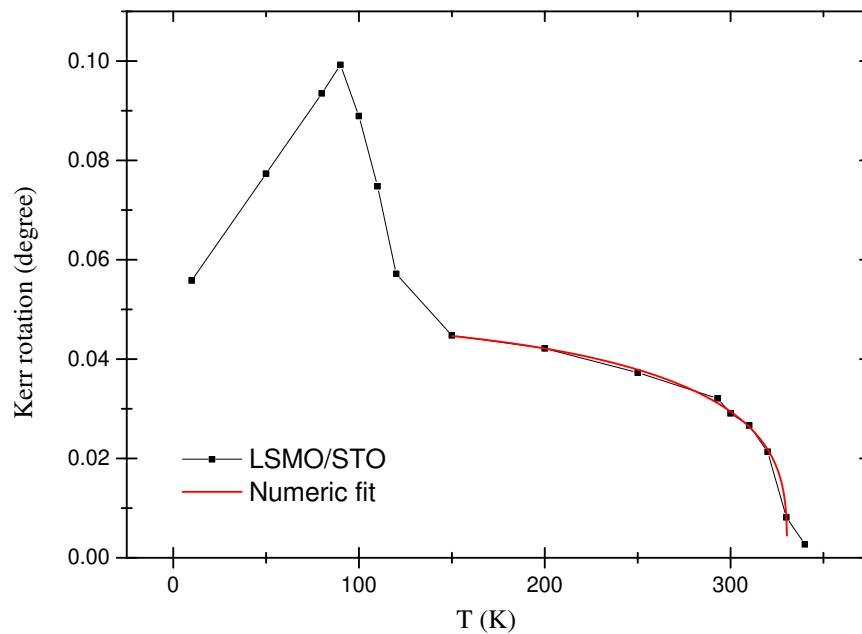

Figure 7.11: The average of the absolute values of Kerr rotation of LSMO/STO between 2.5 - 4 eV as a function of temperature. Experimentally obtained data are fitted with a theoretical model. The theoretical model gives a Curie temperature of 330 K.

Conclusions

The impact of epitaxial strain on thin film LSMO has been studied using magneto-optical methods. Room temperature measurements of MO spectroscopy on four differently strained samples showed deterioration of magnetic properties with increasing epitaxial strain. Two already reported transitions at around 2.4 eV and 3.6 eV have been observed on all samples. The numeric calculation of the off-diagonal elements of the permittivity tensor has been carried out from the measured MOKE and using spectroscopic ellipsometry data from literature. The spectra of the off-diagonal permittivity elements revealed a third transition at around 4.3 eV for samples grown under compressive strain.

A wide range of low temperature measurements of the MO Kerr rotation spectra have been carried out for all four samples. The measured spectra of LSMO grown under considerable compressive strain on LAO showed clear magnification of the influence of the third transition at around 4.3 eV. This magnification was less observable on LSMO grown under small compressive strain on LSAT. The samples grown under tensile strain showed no conclusive proof of this transition. The spectra of LSMO grown under large tensile strain on DSO showed no change in spectral shape with temperature and showed very poor magnetic properties for all measured temperatures. The spectra of LSMO grown under small tensile strain on STO showed spectral changes for temperatures around 100 K, where STO undergoes a structural transition from cubic to tetragonal state, thus changing the epitaxial strain.

The dependence of the magnitude of the MO Kerr rotation on temperature was fitted with a theoretical model for three samples, allowing for the approximation of the Curie temperature (see Table 7.1). The model has proven inappropriate for the approximation of the Curie temperature of LSMO deposited on LAO due to it's spin reorientation transition at 200 K.

The measurements of the temperature dependent MO Kerr rotation have revealed the potential for a thorough future investigation. The already planned investigation will focus on the full measurements of the MOKE as well as spectroscopic ellipsometry in order to obtain the temperature dependence of the complete permittivity tensor.

Sample	LSMO/LSAT	LSMO/STO	LSMO/DSO
Lattice mismatch m (%)	0.21	-0.74	-1.67
Curie temperature T_C (K)	356	330	313

Table 7.1: The estimated Curie temperatures from the MO Kerr rotation temperature dependence for three measured samples.

Bibliography

[1] M. Veis, Š. Višňovský, Ph. Lecoeur, A.-M. Haghiri-Gosnet, J.-P. Renard, P. Beauvillain, W. Prellier, B. Mercey, J. Mistrík, and T. Yamaguchi. Magneto-optic spectroscopy of $La_{2/3}Sr_{1/3}MnO_3$ films on $SrTiO_3$ ($1\,0\,0$) and ($1\,1\,0$) substrates. *Journal of Physics D: Applied Physics*, 42(19):195002, September 2009.

[2] R. Rauer, G. Neuber, J. Kunze, J. Bäckström, M. Rübhausen, T. Walter, and K. Dörr. Magneto-optical investigation of spin polarisation of $La_{0.7}Ca_{0.3}MnO_3$ and $La_{0.7}Sr_{0.3}MnO_3$. *Journal of Magnetism and Magnetic Materials*, 290-291:948–951, April 2005.

[3] H. L. Liu, K. S. Lu, M. X. Kuo, L. Uba, S. Uba, L. M. Wang, and H.-T. Jeng. Magneto-optical properties of $La_{0.7}Sr_{0.3}MnO_3$ thin films with perpendicular magnetic anisotropy. *Journal of Applied Physics*, 99(4):043908, February 2006.

[4] R. von Helmolt, J. Wecker, B. Holzapfel, L. Schultz, and K. Samwer. Giant negative magnetoresistance in perovskitelike $La_{2/3}Ba_{1/3}MnO_x$ ferromagnetic films. *Physical Review Letters*, 71(14):2331–2333, October 1993.

[5] G.H. Jonker and J.H. Van Santen. Ferromagnetic compounds of manganese with perovskite structure. *Physica*, 16(3):337–349, March 1950.

[6] M. Bowen, M. Bibes, A. Barthélémy, J.-P. Contour, A. Anane, Y. Lemaitre, and A. Fert. Nearly total spin polarization in $La_{2/3}Sr_{1/3}MnO_3$ from tunneling experiments. *Applied Physics Letters*, 82(2):233–235, January 2003.

[7] Clarence Zener. Interaction between the d-shells in the transition metals. II. ferromagnetic compounds of manganese with perovskite structure. *Physical Review*, 82(3):403–405, May 1951.

[8] James M. Rondinelli, Steven J. May, and John W. Freeland. Control of octahedral connectivity in perovskite oxide heterostructures: An emerging route to multifunctional materials discovery. *MRS Bulletin*, 37(3):261–270, March 2012.

[9] B. Sedlák and I. Štoll. *Elektřina a magnetismus*. Karolinum, Prague, third edition, January 2013. ISBN 9788024621982.

[10] L.D. Landau and E.M. Lifshitz. *Electrodynamics of Continuous Media*. Pergamon Press, Tarrytown, second edition, 1984. ISBN 9780080302751.

[11] P. S. Pershan. Magneto-optical effects. *Journal of Applied Physics*, 38(3): 1482–1490, 1967.

[12] H.S. Bennett and E.A. Stern. Faraday effect in solids. *Physical Review*, 137: A448–A461, January 1965.

[13] M. Born and E. Wolf. *Principles of Optics*. Pergamon Press, Oxford, sixth edition, 1980. ISBN 9780080264820.

[14] L. Motl and M. Zahradník. *Pěstujeme lineární algebru*. Karolinum, Prague, 1995. ISBN 8071841862.

[15] Miroslav Nývlt. *Optical interactions in ultrathin magnetic film structures*. PhD thesis, Prague, August 1996.

[16] Štefan Višňovský. *Optics in magnetic multilayers and nanostructures*. CRC Taylor & Francis, Boca Raton, March 2006. ISBN 9780849336867.

[17] Pochi Yeh. Optics of anisotropic layered media: A new 4 x 4 matrix algebra. *Surface Science*, 96(1):41 – 53, 1980.

[18] Martin Zahradník, Thomas Maroutian, Martin Zelený, Lukáš Horák, Georg Kurij, Tomáš Maleček, Lukáš Beran, Štefan Višňovský, Guillaume Agnus, Philippe Lecoeur, and Martin Veis. Electronic structure of $La_{2/3}Sr_{1/3}MnO_3$: Interplay of oxygen octahedra rotations and epitaxial strain. *Physical Review B*, 99(19), May 2019.

[19] J. M. D. Coey. *Magnetism and magnetic materials*. Cambridge University Press, Cambridge New York, 2009. ISBN 9780511845000.

[20] Soshin Chikazumi. *Physics of ferromagnetism*. Oxford University Press, Oxford New York, 2009. ISBN 9780199564811.

[21] B. D. Cullity. *Introduction to magnetic materials*. Addison-Wesley Pub. Co, Reading, Mass, 1972. ISBN 0-201-01218-9.

[22] A-M Haghiri-Gosnet and J-P Renard. CMR manganites: physics, thin films and devices. *Journal of Physics D: Applied Physics*, 36(8):R127–R150, April 2003.

[23] A. Vailionis, H. Boschker, W. Siemons, E. P. Houwman, D. H. A. Blank, G. Rijnders, and G. Koster. Misfit strain accommodation in epitaxial ABO_3 perovskites: Lattice rotations and lattice modulations. *Physical Review B*, 83(6), February 2011.

[24] Michael C. Martin, G. Shirane, Y. Endoh, K. Hirota, Y. Moritomo, and Y. Tokura. Magnetism and structural distortion in the $La_{0.7}sr_{0.3}mno_3$ metallic ferromagnet. *Physical Review B*, 53(21):14285–14290, June 1996.

[25] Martin Zahradník. *Dynamic control of magnetization for spintronic applications studied by magneto-optical methods*. PhD thesis, Charles University, Prague, June 2019.

[26] A. Khapikov, L. Uspenskaya, I. Bdikin, Ya. Mukovskii, S. Karabashev, D. Shulyaev, and A. Arsenov. Magnetic domains and twin structure of the $La_{2/3}Sr_{1/3}MnO_3$ single crystal. *Applied Physics Letters*, 77(15):2376–2378, October 2000.

[27] F. Tsui, M. C. Smoak, T. K. Nath, and C. B. Eom. Strain-dependent magnetic phase diagram of epitaxial $La_{0.67}Sr_{0.33}MnO_3$ thin films. *Applied Physics Letters*, 76(17):2421–2423, April 2000.

[28] Xiaoyan Li, Ionela Lindfors-Vrejoiu, Michael Ziese, Alexandre Gloter, and Peter A. van Aken. Impact of interfacial coupling of oxygen octahedra on ferromagnetic order in $La_{0.7}Sr_{0.3}MnO_3/SrTiO_3$ heterostructures. *Scientific Reports*, 7(1), January 2017.

[29] Zhipeng Li, Dongsheng Song, Rong Yu, Binghui Ge, Zhenyu Liao, Yueliang Li, Shuai Dong, and Jing Zhu. Competing interfacial reconstruction mechanisms in $La_{0.7}Sr_{0.3}MnO_3/SrTiO_3$ heterostructures. *ACS Applied Materials & Interfaces*, 8(36):24192–24197, September 2016.

[30] Martin Veis. *Optical interactions in thin films of selected magnetic oxides.* PhD thesis, Charles University, Prague, March 2009.

[31] S. Yamaguchi, Y. Okimoto, K. Ishibashi, and Y. Tokura. Magneto-optical kerr effects in perovskite-type transition-metal oxides: $La_{1-x}Sr_xMnO_3$ and $La_{1-x}Sr_xCoO_3$. *Physical Review B*, 58(11):6862–6870, September 1998.

[32] Bao-Min Ma and K.S.V.L. Narasimhan. Temperature dependence of magnetic properties of Nd-Fe-B magnets. *Journal of Magnetism and Magnetic Materials*, 54-57:559–562, February 1986.

[33] K.J. Strnat, D. Li, and H. Mildrum. High and low temperature properties of sintered Nd-Fe-B magnets. *International Workshop on Rare Earth Magnets and Their Applications*, May 1985.

[34] L. M. García, J. Chaboy, F. Bartolomé, and J. B. Goedkoop. Orbital magnetic moment instability at the spin reorientation transition of $Nd_2Fe_{14}B$. *Physical Review Letters*, 85(2):429–432, July 2000.

[35] A. K. Zvezdin. *Modern magnetooptics and magnetooptical materials.* Institute of Physics Pub., Bristol Philadelphia, Pa., 1997. ISBN 978-0750303620.

[36] Farrel W. Lytle. X-ray diffractometry of low-temperature phase transformations in strontium titanate. *Journal of Applied Physics*, 35(7):2212–2215, July 1964.

List of Figures

List of Abbreviations

CMR	-	colossal magnetoresistance
DE	-	double-exchange
DSO	-	$DyScO_3$
LAO	-	$LaAlO_3$
LSAT	-	$(LaAlO_3)_{1/3}(Sr_2AlTaO_6)_{2/3}$
LSMO	-	$La_{2/3}Sr_{1/3}MnO_3$
MO	-	magneto-optical
MOKE	-	magneto-optical Kerr effect
NGO	-	$NdGaO_3$
OOC	-	oxygen octahedra coupling
OOR	-	oxygen octahedra rotations
PLD	-	pulsed laser deposition
RAE	-	rotating analyzer ellipsometry
RCE	-	rotating compensator ellipsometry
SE	-	spectroscopic ellipsometry
STO	-	$SrTiO_3$

A. Attachments

A.1   RCE intensity calculation

Following from (4.9):

$$J_p = (\cos^2 c - i\sin^2 c)\sin\Psi e^{i\Delta} - (1+i)\cos c\sin c\cos\Psi\,, \qquad (A.1)$$

using the identities

$$\cos^2 c + i\sin^2 c = \frac{1}{2}(1+i)(\cos(2c) - i)\,, \qquad (A.2)$$

$$2\cos\alpha\sin\alpha = \sin(2\alpha)\,, \qquad (A.3)$$

we get

$$J_p = \frac{1}{2}(1+i)[\cos(2c)\sin\Psi e^{i\Delta} - i\sin\Psi e^{i\Delta} - sin(2c)\cos\Psi]\,. \qquad (A.4)$$

If we now take the square of the absolute value of (A.4) the prefactor $1/2(1+i)$ will be one half and the rest of the equation will be

$$2I = + \cos^2(2c)\sin^2\Psi + \sin^2\Psi + \sin^2(2c)\cos^2\Psi +$$
$$+ i\sin^2\Psi\cos(2c) - \sin(2c)\cos(2c)\sin\Psi\cos\Psi e^{i\Delta} -$$
$$- i\sin^2\Psi\cos(2c) + i\sin\Psi\cos\Psi\sin(2c)e^{i\Delta} -$$
$$- \sin(2c)\cos(2c)\sin\Psi\cos\Psi e^{-i\Delta} - i\sin\Psi\cos\Psi\sin(2c)e^{-i\Delta}\,. \qquad (A.5)$$

Through some cancellations, the repeated use of (A.3) and the identity

$$e^{i\alpha} = \cos\alpha + i\sin\alpha\,, \qquad (A.6)$$

we get

$$2I = + \cos^2(2c)\sin^2\Psi + \sin^2\Psi + \sin^2(2c)\cos^2\Psi +$$
$$- \frac{1}{2}\sin(4c)\sin(2\Psi) - \sin(2\Psi)\sin(2c)\sin\Delta\,. \qquad (A.7)$$

Using the double angle identities

$$\cos^2 c = \frac{1}{2}(1+\cos(2c))\,, \qquad (A.8)$$

$$\sin^2 c = \frac{1}{2}(1-\cos(2c))\,, \qquad (A.9)$$

we can rewrite the intensity (A.7) as

$$2I = +\frac{1}{4}(1 - \cos(2\Psi))(1 + \cos(4c)) + \frac{1}{2}(1 - \cos(2\Psi)+$$

$$+\frac{1}{4}(1 - \cos(4c))(1 + \cos(2\Psi))$$

$$-\frac{1}{2}\sin(4c)\sin(2\Psi) - \sin(2\Psi)\sin(2c)\sin\Delta\,. \tag{A.10}$$

Finally if we rearrange the equation, multiply it by 2 and introduce the amplitude of intensity I_0 we can rewrite the relation as

$$I = I_0[2 - \cos(2\Psi) - 2\sin(2\Psi)\sin(\Delta)\sin(2c) - \cos(2\Psi)\cos(4c) - \sin(2\Psi)\cos(\Delta)\sin(4c)]\,. \tag{A.11}$$

A.2 MO spectroscopy intensity calculation

The Jones vector for the MO spectroscopy set-up is from (4.16)

$$\boldsymbol{J}^{(O)} = \begin{bmatrix} -e^{i\Gamma}\Phi_k\cos^2\zeta - \sin\zeta\cos\zeta \\ -e^{i\Gamma}\Phi_k\sin\zeta\cos\zeta - \sin^2\zeta \end{bmatrix}\,. \tag{A.12}$$

If we take the square of it's absolute value we get

$$I = |\Phi_k|^2\cos^4\zeta + \sin^2\zeta\cos^2\zeta + \Phi_k e^{i\Gamma}\cos^3\zeta\sin\zeta + \overline{\Phi}_k e^{-i\Gamma}\cos^3\zeta\sin\zeta+$$
$$+ |\Phi_k|^2\cos^2\zeta\sin^2\zeta + \sin^4\zeta + \Phi_k e^{i\Gamma}\cos\zeta\sin^3\zeta + \overline{\Phi}_k e^{-i\Gamma}\cos\zeta\sin^3\zeta\,. \tag{A.13}$$

Using (A.3), the following identity for the sine and cosine function and the identity for complex conjugate

$$\cos^2 x + \sin^2 x = 1\,, \tag{A.14}$$
$$z + \overline{z} = 2\operatorname{Re}\{z\}\,, \tag{A.15}$$

yields

$$I = \sin^2\zeta + |\Phi_k|^2\cos^2\zeta + \sin(2\zeta)\operatorname{Re}\left\{\Phi_k e^{i\Gamma}\right\}\,. \tag{A.16}$$